3

4   **Title: Nanolattices - An Emerging Class of Mechanical Metamaterials**

5   *Jens Bauer*, Lucas R. Meza, Tobias A. Schaedler, Ruth Schwaiger, Xiaoyu Zheng, Lorenzo*
6   *Valdevit*

7

8   Dr. J. Bauer, Prof. L. Valdevit
9   Department of Mechanical and Aerospace Engineering, University of California Irvine,
10   CA 92697, USA
11   E-mail: jens.bauer@uci.edu

12   Dr. J. Bauer, Dr. R. Schwaiger
13   Institute for Applied Materials, Karlsruhe Institute of Technology,
14   Hermann-von-Helmholtz-Platz 1, Eggenstein-Leopoldshafen, 76344, Germany

15   Dr. L. R. Meza
16   Engineering Department, Trumpington Street, Cambridge, CB2 1PZ, UK

17   Dr. T. A. Schaedler
18   HRL Laboratories Limited Liability Company, Malibu, CA 90265, USA

19   Prof. X. Zheng
20   Department of Mechanical Engineering, Virginia Tech,
21   445 Goodwin Hall,635 Prices Fork Road - MC 0238, Blacksburg, VA 24061, USA

23

24

25   **In 1903 Alexander Graham Bell developed a design principle to generate lightweight,**

26   **mechanically robust lattice structures based on triangular cells; this has since found**

27   **broad application in lightweight design. Over one hundred years later, the same principle**

28   **is being used in the fabrication of nanolattice materials, namely lattice structures**

29   **comprised of nanoscale constituents. Taking advantage of size-dependent properties**

30   **typical of nanoparticles, nanowires, and thin films, nanolattices redefine the limits of the**

31   **accessible material property space throughout different disciplines. We review the**

32   **exceptional mechanical performance of nanolattices, including their ultra-high strength,**

33   **damage tolerance, and stiffness, and examine their potential for multifunctional**

34   **applications beyond mechanics. The efficient integration of architecture and size-affected**

35   **properties is key to further develop nanolattices. The introduction of hierarchical**

36   **architecture is an effective tool in enhancing mechanical properties, and the eventual goal**

37   **of nanolattice design may be to replicate the intricate hierarchies and functionalities**

38   **observed in biological materials. Additive manufacturing and self-assembly techniques**

39   **enabled lattice design at the nanoscale, the scaling-up of nanolattice fabrication is**

40   **currently the major challenge to their widespread use in technological applications.**

41

1. Introduction

No solid material considerably lighter than water has been reported to date. To decrease density beyond this point, materials must have a porosity, which generally comes at the cost of a disproportional degradation of properties. For example, a foam with a relative density ($\bar{\rho}$), i.e. the volume fraction, of 10% will have a stiffness and strength that are 0.3% and 0.9% of the constitutive bulk material, respectively. In this sense, lighter than water and as strong as steel is intuitively a utopian property combination, yet it has recently been achieved with nanolattice materials.[1–3]

Material availability and advances in processing have defined human progress since the Stone Age, the modern frontier for material design is that of nanomaterials. One- and two-dimensional nanomaterials, such as nanowires and thin films, are known to have exceptional properties, which are intrinsically coupled to dimensional constraints such as surface-to-volume ratios. When nanowires and thin films are scaled up, their size-affected properties are lost. Similarly, when they are clustered in a composite, interfaces weaken their overall performance. To overcome this dilemma one could think of highly ordered three-dimensional architectures constructed from nanowires or thin films. This is what long remained technologically infeasible - this is what nanolattice materials are.

Nanolattices have been rapidly developed over the past few years, redefining the limits of the accessible material property space. The key driving force for this advance was the evolution of high-precision additive manufacturing techniques, such as self-propagating photopolymer waveguides (SPPW)[4], projection micro-stereolithography (PμSL)[5], and direct laser writing (DLW)[6,7], which have led to the production of progressively smaller lattice structures **(Figure 1)** reaching unit cell sizes below 1 μm.[8] Self-assembly techniques have been used to synthesize nanolattices with unit cell sizes down to the order of 50 nm.[2,3,9] Genetic engineering may be

66 another potential method for nanolattice fabrication.[10–12] Micro- and nanolattices possess

67 unparalleled mechanical properties at extremely low densities, including effective strengths of

68 up to 1 GPa[1–3,9,13,14], high deformability and recoverability with brittle constituent

69 materials[13,15–18], and ultra-high stiffness[19], all despite being comprised of 50-99.9% air. Also,

70 auxetic structures with negative Poisson's ratio[20], pentamode lattices with near zero shear

71 modulus and a resulting fluid-like behavior[21], and exceptional non-mechanical properties,

72 such as optical cloaking[22,23] and broadband electromagnetic polarization[24], have been

73 demonstrated.
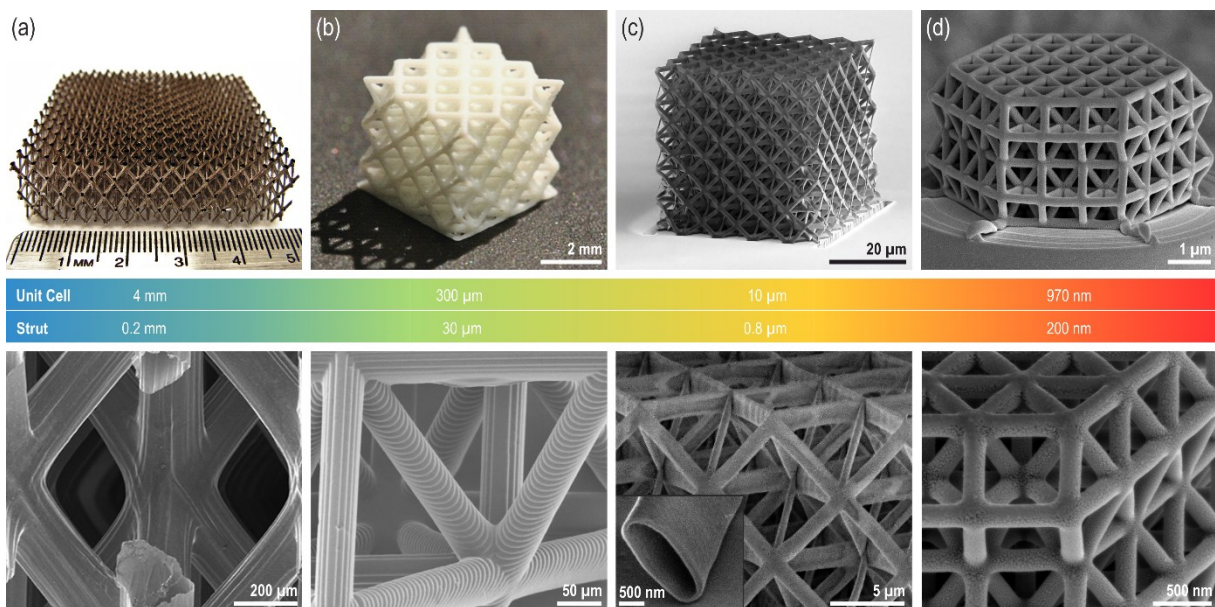
74

75 **Figure 1**. **Lattice miniaturization – from the millimeter- to the nanoscale.** Characteristic
76 unit cell dimensions and diameters of individual struts are indicated. (a) Hollow-beam nickel
77 lattice, manufactured using SPPW polymer templates, electroless nickel plating, and base
78 etching to remove the polymer. (b) Solid-beam alumina lattice fabricated by PµSL with a
79 nanoparticle loaded resist and subsequent sintering. (c) Hollow-beam alumina lattice fabricated
80 by DLW, atomic layer deposition and oxygen plasma etching. (d) Solid-beam glassy carbon
81 lattice made by DLW and subsequent pyrolysis. Adopted from [1] and reproduced with
82 permission, [15] 2011, [19] 2014, [13] 2014, The American Association of the Advancement of
83 Science.

84 While the concept of resilient lattice architecture is more than a century old and goes back to

85 Alexander Graham Bell[25] and Buckminster Fuller[26], today lattices can for the first time be

86 made small enough to actually exploit nanoscale properties. It is this unique feature, which

87 facilitates extraordinary strength, sometimes higher than that of the corresponding fully dense

88 bulk material, as well as optical or electromagnetic properties. Other mechanical characteristics

89 of nanolattices, including ductile-like behavior and high stiffness, arise from scale-independent

90 structural effects.

91 At the nanoscale, *size effects* can tremendously alter the mechanical[27–31], magnetic[27],

92 thermal[32,33], and electrical[34,35] properties of a material compared to its corresponding bulk

93 behavior. This is related to microstructural constraints, such as the size and distribution of

94 dislocations, grain boundaries, cracks and voids, which in small scales can be affected by

95 dimensional constraints. The presence of defects can have various effects in different materials

96 systems. For example, plastic flow in metals occurs via dislocation motion, and defects such as

97 grain boundaries hinder this process; thus, the yield strength of polycrystalline metals generally

98 increases as the grain size is reduced.[36] The chemical bonds in ceramics do not allow plastic

99 deformation at room temperature, and stress concentrations at crack tips cannot be relieved by

100 localized plastic flow; the size of cracks is therefore the limiting factor for their strength. The

101 size of any defect is limited by the overall dimensions of an object, meaning the smaller the

102 object, the higher its strength will be. Mechanisms governing strength can be more

103 complex[27,30,31], but there is a clear overall trend that "smaller is stronger". Metallic and ceramic

104 ultra-strong nanoscale materials have been reported, such as 40 nm thin and 5.6 GPa strong

105 gold wires[37], 20 nm thin and 18 GPa strong silicon wires[38], and carbon nanotubes (CNTs)

106 and graphene reaching stresses as high as 100–130 GPa[37]. Additionally, properties like

107 ductility in silicon nanowires[38–40] and metallic glass nanopillars[41,42], increased Young's

108 modulus in carbon[43–46] and nanoporous gold[47], as well as notch insensitivity in gold

109 nanowires[48] have also been observed. Future nanolattices may be able to further capitalize on

110 these enhanced nanomaterial properties.

111 Using classical material fabrication methods, there appears to be little room for further

112 expansion of the accessible material property space. To develop new materials, three

113   fundamental approaches have been identified:[49] (I) By manipulation of the *chemistry*, metal

114   alloys, polymer formulations, and ceramic or glass compositions may be developed. (II)

115   Manipulating the *microstructure* by thermo-mechanical processing controls the distribution of

116   defects and phases, thereby modifying a material's properties without changing the chemistry.

117   Searching for lighter, stronger, stiffer, and more durable materials, both approaches have

118   systematically been exploited over centuries with great success. (III) Controlling the

119   *architecture* of multiple materials (composites) or a single material and space (cellular

120   materials) creates hybrid materials. Introducing architecture into materials design allows for the

121   tailoring of a vast range of material property combinations depending on the topology, i.e. the

122   spatial layout of constituent materials.

123   The mechanical properties of cellular materials are defined by their constituent material

124   properties, relative density and architecture, and they are traditionally classified as *bending-* or

125   *stretching-dominated* depending on their topology.[50] Stochastic structures such as foams

126   commonly deform by bending of their ligaments, resulting in an inhomogeneous stress

127   distribution and therefore poor material utilization. The effective strength and stiffness of

128   bending-dominated structures scales with their relative density as $\sigma_{eff} \propto \bar{\rho}^{\,1.5}$ and $E_{eff} \propto \bar{\rho}^{\,2}$

129   respectively.[51] An ideal stretching-dominated material deforms via uniaxial compression and

130   tension of its members, and has a linear scaling with the relative density of both strength ($\sigma_{eff} \propto$

131    $\bar{\rho}$) and stiffness ($E_{eff} \propto \bar{\rho}$).

132   Bending- or stretching-dominated behavior of an open-cell topology generally depends on the

133   rigidity of its pin-jointed counterpart **(Figure 2)**.[52] In 2D, the triangle is the only rigid polygon,

134   and in 3D, polyhedral cells with fully triangulated surfaces are rigid. The connectivity (Z) of a

135   structure, namely the average number of elements connected at a node, is a good indicator of

136   rigidity. A topology constructed from rigid unit cells is necessarily fully rigid and stretching-

137   dominated, with $Z = 6$ and $Z = 12$ for the 2D and 3D cases, respectively (Figure 2a).

138 Topologies with lower connectivities can be periodically-rigid and theoretically still stretching-

139 dominated (Figure 2b-c), but they are more sensitive to imperfections, which may easily

140 activate deformation mechanisms that can cause bending. Non-rigid topologies are fully

141 bending-dominated (Figure 2d). Although valid in many cases, the classification of cellular

142 materials as bending- or stretching-dominated based on their topology does not account for

143 influencing factors such as the loading conditions (Figure 2e) or the shape and rigidity of the

144 nodes, which is of particular relevance for hollow-beam lattices. The topology of a structure

145 may therefore not sufficiently indicate its bending-or stretching-dominated behavior.
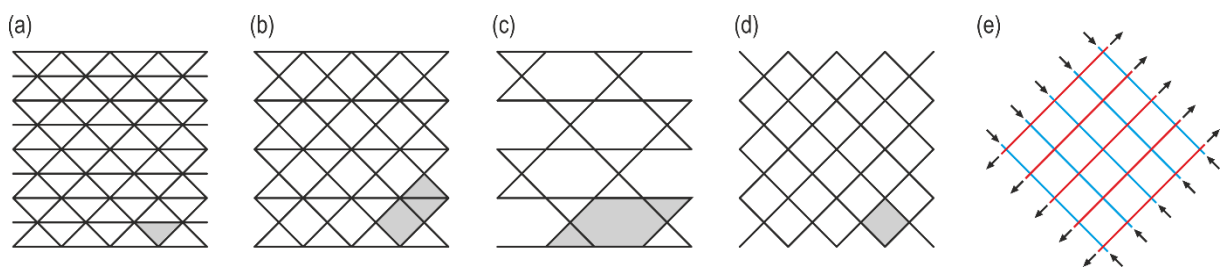
147 **Figure 2. Bending- versus stretching-dominated behavior.** (a) Stretching-dominated, rigid
148 topology (Z=6) constructed from rigid triangular unit cells. (b-c) Periodically-rigid,
149 theoretically stretching-dominated topologies consisting of non-rigid unit cells, (b) Z=5, and
150 (c) Z=4. (d) Non-rigid, generally bending-dominated topology (Z=4) constructed from non-
151 rigid unit cells. (e) Non-rigid topology which for the indicated load case behaves fully
152 stretching-dominated representing the least weight optimum. Unit cells are shaded in gray.

153 Introducing *lattice architecture* into cellular materials can markedly expand the boundaries of

154 accessible material property space, in particular in the low density regime.[49] A lattice material

155 is defined as a periodic network of structural elements such as slender beams or rods.[49] Apart

156 from the obvious case of lattice trusses, this definition includes shell-like designs such as

157 honeycombs. For a lattice to be formally considered a material instead of a structure, the length

158 scale on which a load is applied should be large compared to that of the lattice elements.[49] The

159 most common mechanically investigated lattices are rigid assemblies of octahedron and

160 tetrahedron unit cells, named octet-trusses (see right three structures in Figure 1).[52] Beyond

161 high strength and stiffness at low weight[53,54], lattice architecture offers a range of other

162 exceptional mechanical properties. Some of those properties such as tunable energy

163 absorption[55] can be incorporated in stretching-dominated designs. Others, including tailorable

164 thermal expansion[56], origami-based adaptivity[57], and auxetic[58] or fluid-like behavior[59],

165 involve hinge-like deformation and folding of bending-dominated topologies. These

166 mechanisms are typical of mechanical metamaterials[60–62].

167 The behavior of *metamaterials* is determined by their topology rather than by their composition.

168 Classically, photonic[62–64] and phononic[62,65,66] crystals derive their properties from wave

169 phenomena and therefore strongly depend on the length scale of their patterns. Photonic crystals

170 for optical cloaking[22] are nanolattices designed to direct light of a certain wavelength around

171 an object rather than scattering it; this would not be possible with self-similar lattices at larger

172 scales. By contrast, mechanical metamaterials rely on scale-independent deformation of their

173 unit cells, and self-similar macro- and nanoscale auxetic[67] and pentamode[21,59] metamaterials

174 have been demonstrated.[61]

175 Certain biological lattice architectures consist of nanoscale building blocks, allowing their

176 mechanical properties to benefit from both optimized topology and material size effects **(Figure**

177 **3)**.[68,69] The architecture of diatoms[10,70], a common type of phytoplankton, is nanometer- or

178 even molecular-scale and has been shown to be remarkably strong[71]. Other natural materials

179 such as cancellous bone[72] or Euplectella glass sponges[73] have lattice elements on the scale of

180 millimeters and are comprised of a hierarchically structured constituent material. Cancellous

181 bone grows adaptively according to the loading situation, with the thickness and the orientation

182 of each ligament depending on the magnitude and orientation of loading.[74,75] The resulting

183 structure is an anisotropic network oriented in the direction of the principal tensile and

184 compressive stresses.[75] this architecture is a classic example of a least-weight design.[76,77]

185 Interestingly, these structures behave stretching-dominated despite not being fully triangulated

186 because struts aligned with the principal stress direction experience no bending moment (Figure

187 2d).[75] Hierarchical design of a solid material from nanoscale building blocks allows for the

188   exploitation of extraordinary nanoscale strengths and enables high toughness at the

189   macroscale.[68] On the lowest level of hierarchy, solid bone[72], enamel[78], and nacre[79] consist

190   of ceramic-like elements on the order of 1-100 nm held together by a small volume fraction of

191   a soft organic matrix.

192
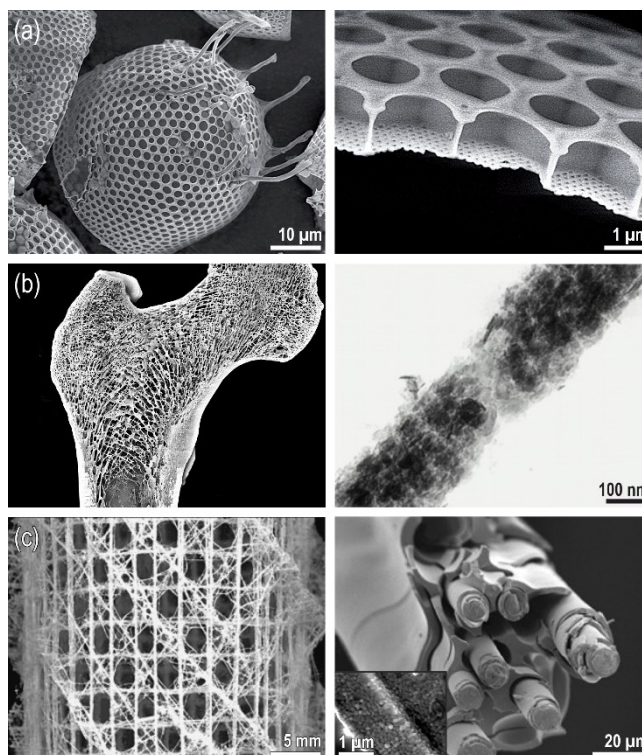
Figure 3. **Biological hierarchical lattice materials gain high mechanical robustness from optimized topologies and mechanical size effects in their nanoscale basic building blocks.** (a) Hierarchical diatom lattice comprised of nanoscale lattice elements. (b) Cancellous bone network (left) whose hierarchical solid material consists of arrays of mineralized collagen fibrils; (right) mineralized collagen fibril of a turkey tendon which is assembled from 2-4 nm thick plate-like crystals. (c) Euplectella glass sponge lattice (left) and its hierarchically structured base material with 25 nm size nanoparticles on the lowest hierarchical level. Reproduced with permission, [80] 2014, The Royal Society of Chemistry, [81] 2017, Karlsruhe Institute of Technology, [72] 1998, Annual Reviews, [73] 2005, The American Association for the Advancement of Science.

Nanolattice materials, or simply *nanolattices*, are a novel class of mechanical metamaterials; their effective properties are determined both by their topology and their nanoscale architecture, through which they are capable of exploiting unique size-affected material properties. The full potential of nanolattices is actively being discovered, and the remarkable properties that have been found to date may just be the tip of the proverbial iceberg. We still cannot mimic the

complex hierarchical architecture of biological materials, and scaling-up nanolattices for use in technological applications without sacrificing their beneficial properties will be one of the futures challenges. Prototypes of bio-inspired multi-scale lattices, up to several centimeters in size, have recently demonstrated exceptional properties[82,83] compared to their first order counterparts[13,19]. While they are still at the outset of their development, nanolattices may eventually lead us to a new era of lighter, stronger, and more durable multifunctional materials.

In this paper, we examine the unique mechanical properties of nanolattices. Key mechanisms governing the behavior are discussed in the context of lattice architecture and size-effects, and shortcomings along with potential avenues for overcoming them are identified. We examine nanolattice performance in relation to large-scale lattice materials, disordered nanoporous materials, and bulk materials to provide a comprehensive review of their materials property space. We further investigate the evolution of nanolattice materials throughout other disciplines, and discuss multifunctionality, relevant fabrication methods, up-scaling approaches, and future directions.

2. Exploiting Nanolattice Architecture

Here we discuss the benefits of combining nanomaterials and lattice architectures with a particular focus on mechanical properties. Properties unique to nanolattices are identified, and their dependence on small-scale materials effects, architecture, or a combination of the two is examined. In this context, not all lattices presented here are fully nanoscale; for properties that rely on scale-independent effects, we discuss where nanoscale structuring may be advantageous for multifunctional reasons and point out where the incorporation of material size effects has the potential to improve properties. We examine which of the presented characteristics can be successfully combined and which ones are incompatible.
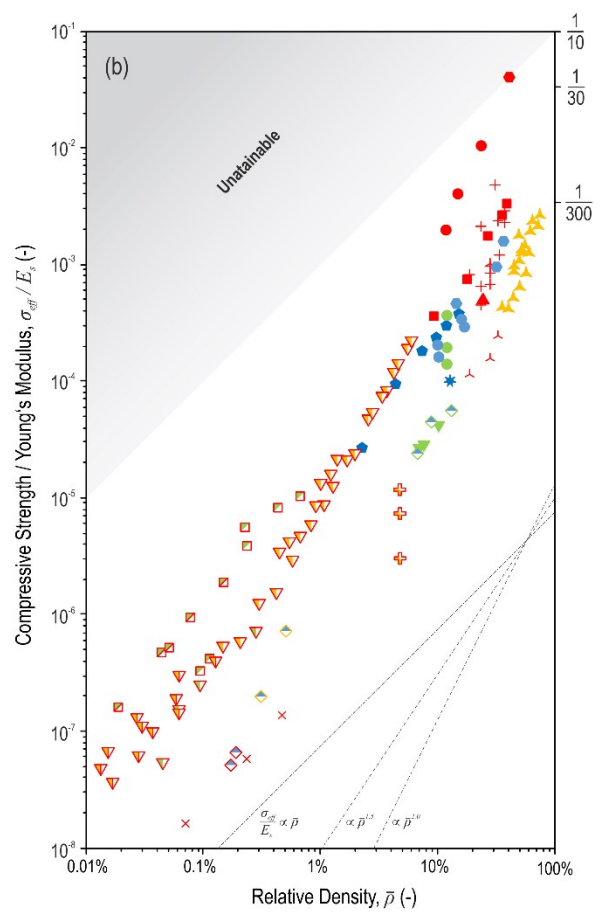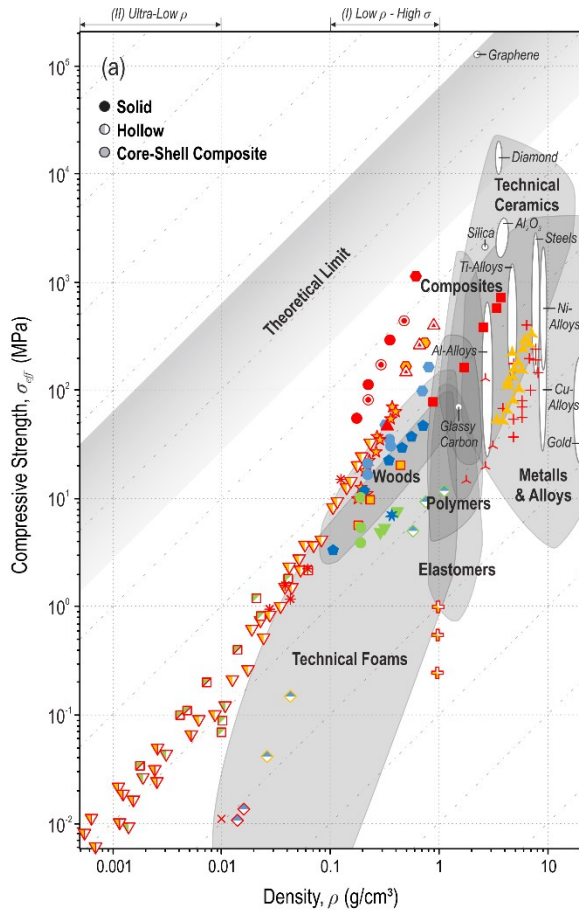
2.1. Strength

232   The strength of a nanolattices is defined by three factors: (I) the architecture, (II) the length

233   scale, which controls the effect of size-dependent strengthening, and (III) the solid material

234   composition and microstructure, which correlate with the fabrication methodology.

235   In the context of lightweight materials design, one of the most important figures of merit to

236   evaluate a material's performance is its specific strength, or the ratio between its strength and

237   density. When considering specific strength, there are ultimately two necessary conditions to

238   justify nanolattice materials and the enormous effort to process them. First, to legitimate the

239   lattice architecture, they must achieve a combination of strength and density which may not be

240   attained by any fully dense material. In relation to the material property space accessible by

241   commercial bulk materials, this is often referred to as reaching the "white space". Second,

242   nanolattice materials must capitalize on strength gains from material size effects, otherwise the

243   same performance can be realized by self-similar macro-scale lattice materials.

244   *2.1.1. The Strength of Existing Nano-, Micro- and Macrolattice Materials*

245   **Figure 4a** shows a compressive strength versus density material property chart comparing

246   different nano-, micro-, and macrolattices as well as stochastic nanoporous foams and

247   commercial bulk materials. Lattices with rigid and non-rigid topologies and with different

248   material compositions are included across all length scales. The dashed diagonal guidelines

249   represent materials that have the same specific strength. Correspondingly, the theoretical limit

250   bound is defined using diamond, which has the highest specific strength of all bulk materials,

251   and graphene[44], which exhibits the highest strength measured to date.

11
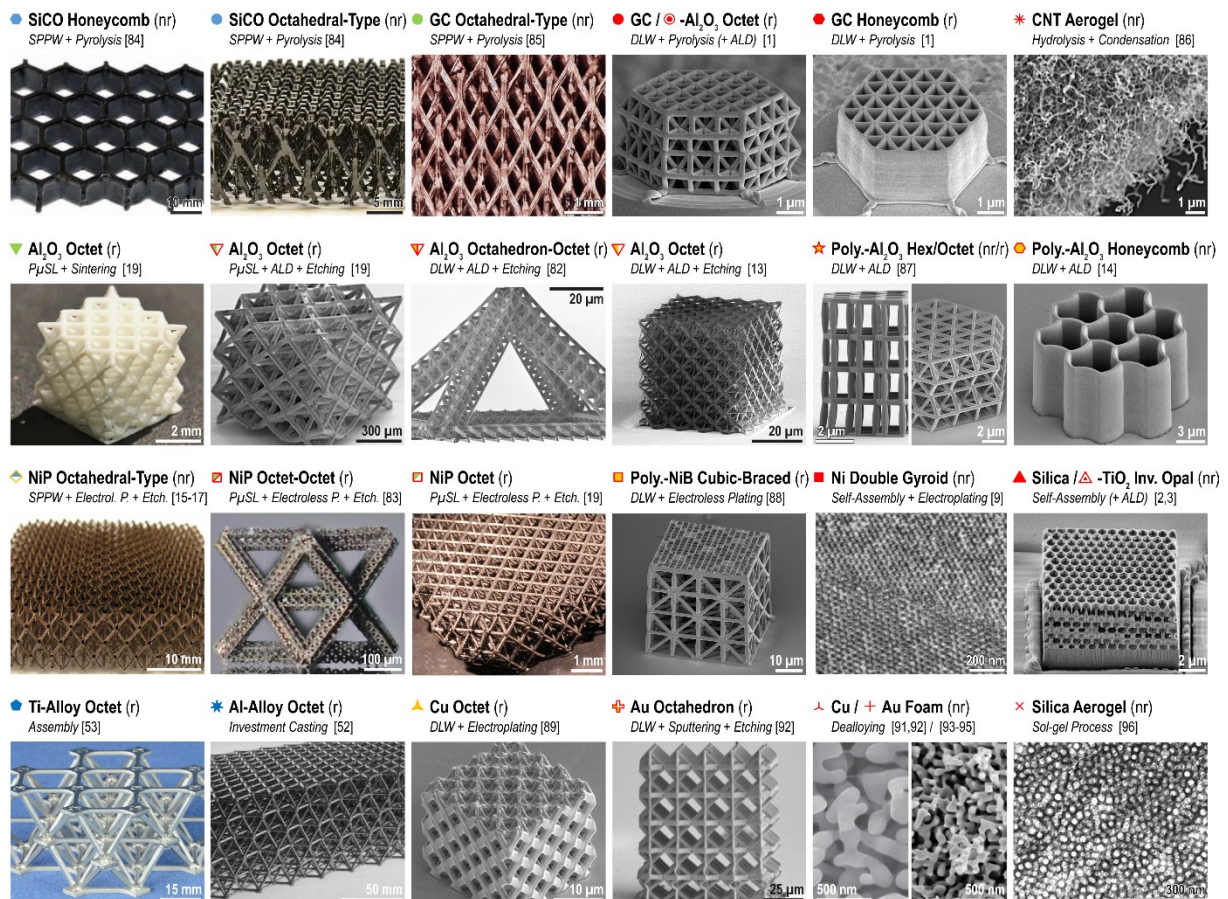
[84]	[84]	[85]	[1]	[1]	[86]
[19]	[19]	[82]	[13]	[87]	[14]
[15–17]	[83]	[19]	[88]	[9]	[2,3]
[53]	[52]	[89]	[90]	[91,92] / [93–95]	[96]

253

Figure 4. Compressive strength-density materials property chart of different nano-, micro-, and macrolattices as well as stochastic nanoporous and commercial bulk materials. Symbol shapes relate to the constituent material, symbol colors indicate the length scale of structuring (fillings = feature diameter, lines = shell thickness, if any). (a) Absolute strength vs. density plot showing that many nanolattices reach far into the low-ρ-high-σ, or the ultralow-ρ "white space". (b) Strength normalized by Young's modulus vs. relative density plot, showing that nanolattice materials are capable of exploiting material strengths up to the theoretical limit ($E_s/10$), whereas the bulk material strengths are often on the order of $E_s/300$. For all structures the rigidity of the topology (r = rigid, nr = non-rigid) as well as a brief description of the applied fabrication process is given. For graphene[44] the tensile strength is shown. Images adopted from [1,14,82,83] and reproduced with permission, [84] 2016, [13,19] 2014, [15] 2011, The American Assosiation for the Advancement of Science, [9] 2017, [3] 2016, [53,89] 2015, [85] 2011, [94] 2007, [52] 2001, Elsevier, [97] 2007, [98] 1998, American Chemical Society, [87] 2016, John Wiley and Sons, [90] 2015, American Society of Mechanical Engineering, [92] 2006, Cambridge University Press.

Overall, the specific strength of the lattice materials presented here roughly increases with decreasing structural length scale. This is demonstrated using a color scale, where materials with larger features are blue and those with smaller features are red. Depending on their material composition, some of the nanolattices reach far into the chart's "white spaces". The impact of architecture is evident when comparing different carbon-based or hollow-beam nickel data, where the strength of stochastic nanoporous materials and lattices with non-rigid topologies falls short of the strength of rigidly architected lattices of similar size.

Two distinct density regimes best illustrate the enhanced performance of nanolattices. (I) In the range of 0.1-1 g/cm³, glassy carbon nanolattices[1], self-assembled core-shell silica-titania inverse opals[2,3], and core-shell polymer-alumina honeycombs[14] reach strengths of up to 400 MPa. Their strength-to-density ratios clearly outperform those of all bulk metals and alloys, polymers, technical and biological cellular materials as well as micro- and macrolattices and nanoporous foams. Glassy carbon honeycombs[1] even reach strengths above 1000 MPa, leaving diamond as the only bulk material with a notably higher ratio of strength-to-density.

283 (II) In the ultra-low density regime, below 0.01 g/cm³, hollow-beam octet lattices comprised of

284 alumina shells on the order of 5-50 nm thickness are up to ten times lighter than the lightest

285 technical foams yet they still achieve strength-to-density ratios comparable to wood and certain

286 aluminum alloys.[13,82] These nanolattices are often built using multi-scale architecture[82,83]

287 (Section 4), and they outperform other ultra-low density materials such as nanoporous silica

288 aerogels[96] and hollow-beam nickel lattices fabricated by SPPW[15] by a factor of more than 10.

289 Reaching into the material property "white spaces" is not limited to nanolattices, as

290 demonstrated by hollow-beam nickel and alumina lattices[19,83], which have notably larger

291 dimensions than nanolattices but maintain similar or greater strengths. Any architected material

292 made of a strong enough constituent material is capable of reaching into new material property

293 spaces, as the diagonal guidelines in Figure 4a indicate. Nanolattices such as self-assembled

294 nickel gyroids[9], core-shell polymer-nickel composite lattices[88] or hollow-beam gold

295 lattices[90] have comparable or lower strengths than bulk materials of equal density despite their

296 small dimensions.

297 To visualize the strength gain of nanolattice materials compared to larger-scale cellular

298 materials and bulk solids, we normalize the data of Figure 4a with the constituent solid materials

299 Young's moduli[3,19,51,53,84,99–101] (E_s) in Figure 4b. Core-shell composite lattices are excluded

300 from this analysis as samples have varying constituent material ratios and therefore cannot be

301 correlated to equivalent bulk materials. The guidelines $\left(\sigma_{eff}/E_s\right) \propto \bar{\rho}$, $\left(\sigma_{eff}/E_s\right) \propto \bar{\rho}^{1.5}$ and

302 $\left(\sigma_{eff}/E_s\right) \propto \bar{\rho}^2$, indicate different scaling laws classically associated with stretching-,

303 bending- and buckling governed behavior, respectively. As a point of reference, the strength of

304 ductile bulk metals is typically on the order of $\sigma_s \sim E_s/300$[51], and brittle materials such as

305 ceramics typically have a yield strain well below 1%[102], for which Hooke's law gives strengths

306 on the order of $\sigma_s \sim E_s/100$.

307   In the range of $\bar{\rho} > 10\%$, nanolattices substantially outperform both macroscale cellular

308   materials and the corresponding fully dense bulk solids from which they derive their properties.

309   Glassy carbon nanolattices achieve up to 400% of the compressive strength of bulk glassy

310   carbon[99] even though their relative density is only 10-25%. Glassy carbon honeycombs resist

311   compressive stresses 16 times as high as the corresponding bulk material at a relative density

312   of 44%. Self-assembled nickel gyroids reach strengths in the range of $E_s/300$ at about 40%

313   relative density. At these high relative densities, the relative contribution of nanoscale size-

314   effects to the strength is much greater than that from the architecture. This is best illustrated

315   with stochastic nanoporous gold, which as well reaches strengths on the order of $E_s/300$ at

316   relative densities of 20-40%.[93–95] Despite their rigid topology, the strength of glassy carbon

317   and hollow-beam alumina nanolattices as well as copper microlattices scale with relative

318   density by the power of >1.5, underperforming the prediction for stretching-dominated

319   material strength.[1,13,89]

320   For lower relative densities of $\bar{\rho} \leq 1\%$ the architecture has a more significant impact on the

321   strength and the effect of the length scale is less apparent. The strengths of both micro- and

322   nanolattices with rigid topologies in this density regime scale linearly with the relative density,

323   clearly outperforming lattices and nanoporous materials with non-rigid topologies. The

324   guidelines in Figure 4b can be used to estimate that the constituent materials' strengths are

325   approximately equal to the corresponding bulk material strength. It is noted that essentially all

326   lattices with $\bar{\rho} \leq 1\%$ are made from hollow shells with nanoscale thickness; no macroscale

327   lattice has been reported that is capable of achieving this scaling at ultra-light weights.
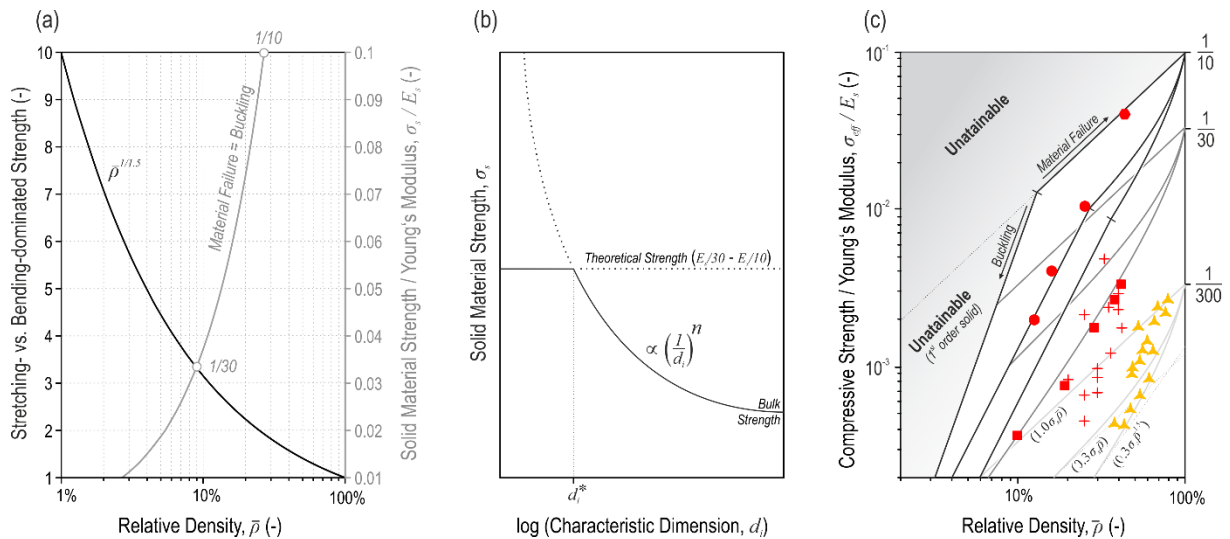
328   *2.1.2. Architecture and Strength*

329   The impact of architecture on the strength of a lightweight material is independent of any length

330   scale effects. **Figure 5a** shows the ratio between ideal stretching- and bending-dominated

331   strength which increases exponentially with decreasing relative density. For lattices with $\bar{\rho} >$

332   10%, which corresponds to the strongest nanolattices, the strength gain of stretching- compared

333   to bending-dominated behavior is less than three; this rises to above a factor of 30 in the ultra-

334   low density regime below $\bar{\rho} = 0.1\%$. The effective strength of cellular materials (σ_{eff}) can be

335   approximated by the first order scaling law

336   $$\sigma_{eff} = C\bar{\rho}^a \sigma_s,$$ (1)

337   where σ_s is the constituent solid material strength, C is a geometric parameter, and the exponent

338   a is 1 for stretching- and 1.5 for bending-dominated behavior.[50] For many near-isotropic

339   cellular topologies, such as the octet lattice and open-cell foams, $C \approx 0.3$ has been found

340   analytically and empirically.[51,52] The normalized strength of glassy carbon nanolattices with

341   $\bar{\rho} \approx 25\%$ whose architecture is designed to be stretching-dominated is about six times higher

342   than that of nickel gyroids of comparable relative density with a non-rigid topology (Figure 4b).

343   Based on Figure 5a, the architecture contributes to approximately a factor of two to this strength

344   difference, meaning a factor of three can be attributed to the difference in constituent materials.

345   In real structures, the difference between strengths likely has a greater dependence on material

346   compositions, meaning architecture has a less significant impact on the effective strength for

347   high relative density materials. In contrast, rigidly designed nickel lattices with $\bar{\rho} \approx 0.3\%$[19]

348   are 20 times stronger than those with non-rigid topologies[16]; from Equation **1**, this difference

349   is almost entirely due to the architecture.

Figure 5. The impact of architecture and size effects on the strength of nanolattice materials. (a) The strength gain of stretching- over bending-dominated behavior increases exponentially with decreasing relative density *(black curve)*. Buckling before material failure becomes increasingly critical with a growing ratio of strength-to-Young's modulus (σ_s/E_s) of a lattice's solid material; the *gray curve* shows the transition between Euler beam buckling and material failure of an ideal solid beam octet lattice with rigid joints. (b) Schematic representation of size-dependent material strengthening. (c) Normalized effective strength (σ_{eff}/E_s) vs. relative density material property chart showing the interaction of size-dependent material strengthening and architectural instability. The cellular material bounds for σ_s of $E_s/300$, $E_s/30$, and $E_s/10$ are shown. See Figure 4 for data point legend.

Increasing the anisotropy of a topology can lead to a strength increase of a factor of up to three. Geometric parameters of $C > 0.3$ can be reached when lattice elements are added, removed, or varied in diameter, or when unit cells are stretched corresponding to a preferred loading direction.[14,90,103] Due to the effects of anisotropy, lattices with non-rigid designs can have strengths comparable to rigid architectures and may outperform them in some cases. For example, lattices with stretched hexagonal-prismatic unit cells were shown to have a 20% increased strength compared to regular octet lattices.[87] Values of $C = 1$ and $a = 1$ correspond to the Voigt bound (Equation 1), which represents the maximum theoretical effective strength for any cellular material. It can be achieved when the entire solid material of a structure is aligned with the direction of an applied load and therefore is stressed uniformly, such as for ideal honeycombs under out-of-plane loading or a square lattice under biaxial loading (Figure 2e). Values of $C < 1$ arise due to the misalignment of lattice elements with respect to an applied

17

373 load. In practice, bending of lattice elements, imperfections, Poisson expansion, instability

374 effects, and experimental misalignment result in additional knockdown of this geometric

375 prefactor.

376 At sufficiently low relative densities, lattice elements may be slender enough to collapse by

377 elastic buckling before reaching the material strength. The effective strength can then be

378 obtained by replacing σ_s in Equation **1** with the elastic buckling strength of a lattice element

379 (σ_{eb}). The Euler buckling criterion of a slender beam is $\sigma_{eb} = k^2\pi^2 I E_s/(Al^2)$, where E_s is the

380 Young's modulus of the solid material, I is the area moment of inertia, A is the lattice elements

381 cross section, and l is its length.[51,53,104] The constant k depends on the boundary conditions

382 and is equal to 2 for rigidly jointed beams and 1 for pin-jointed beams. For a honeycomb wall

383 under out-of-plane loading, the buckling strength relationship $\sigma_{eb} = K E_s L/(1 - v_s^2)$ is valid,

384 where v_s is the Poisson's ratio of the constituent material, L is the width of the cell wall, and K

385 is the constraint factor, which is 2 for the pin-jointed and 6.2 for the clamped case.[51,105]

386 Correspondingly, the effective elastic buckling strength (σ_{eff}^{el}) is given by

387 $$\sigma_{eff}^{el} = D\bar{\rho}^b E_s \tag{2}$$

388 where D is a geometric parameter and the exponent b is 2 for any open-cell material[51] and 3

389 for honeycombs under out-of-plane loading[105]. For stochastic foams $D \approx 0.05$, and for

390 honeycombs $D \approx 6$ has been found.[51,105] For an octet lattice with circular, rigidly connected,

391 solid struts, a geometric parameter of $D \approx 0.123$ can be approximated.[52,53] By relating

392 Equations 1 and 2 it is possible to find the relative density at which the failure mode switches

393 from yielding or fracture to elastic buckling as a function of the ratio between σ_s and E_s (Figure

394 5a).

395 Material instability events like buckling are increasingly relevant for the design of nanolattices.

396 Instability plays a role in the effective strength of a lattice when the constituent material strength

397   is sufficient to prevent failure before the onset of the instability. If we take $\sigma_s \approx E_s/300$, as is

398   the case for many macroscale cellular metals and ceramics, material failure will generally occur

399   well before the onset of any structural instabilities, meaning buckling will not play a role in the

400   lattice strength (Figure 5a). This changes dramatically when the ratio between σ_s and E_s

401   increases. From Equation 2, the failure of a solid-beam octet nanolattice will be governed by

402   elastic buckling below $\bar{\rho} \approx 9\%$ when $\sigma_s = E_s/30$ and below $\bar{\rho} \approx 27\%$ when $\sigma_s = E_s/10$

403   (Figure 5a). Similar relationships can be found for other types of architecture. The high

404   constituent material strength of carbon nanolattices can therefore explain the scaling behavior

405   of their effective strength; the failure of samples with a relative density between 13% and 16%

406   is governed by elastic buckling. Hollow-beam lattices and hierarchical architectures can have

407   significantly improved buckling resistance, facilitating linear scaling of the strength with

408   relative density down to 0.01% (Figure 4b). Shell buckling may still limit the strength of very

409   thin-walled structures, as low density hollow-beam nickel octet microlattices[19] show.

410   As the relative density of a lattice increases beyond ~10%, its elements start to become short

411   and squat, and the first order scaling laws in Equation 1, which are derived assuming lattices

412   consist of slender beams, begin to break down.[51] The theoretical maximum effective strength

413   of an isotropic cellular material can be estimated across all relative densities using the non-

414   linear Hashin-Shtrikman (H-S) bounds[9,106] of

415    $$\sigma_{eff} = \frac{2\bar{\rho}}{\sqrt{4+\frac{11}{3}(1-\bar{\rho})}}\sigma_s \qquad\qquad (3)$$

416   Below $\bar{\rho} \approx 10\%$, Equation 3 can be approximated by the first order scaling relationship in

417   Equation 1 with values of $a = 1$ and $C \approx 0.72$. This maximum strength bound is over two

418   times higher than the ideal relationship predicted for near isotropic lattices, though.[52] Gibson

419   & Ashby have defined the transition between true cellular solids and solids containing isolated

420   pores to be at $\bar{\rho} \approx 30\%$.[51] Above this relative density the non-linear H-S-bounds can be used

421 to explain the scaling behavior, such as of the copper octet lattices and nickel gyroids (Figure

422 5c).

423 The mechanical behavior of hollow-beam and core-shell composite lattices is not always well

424 captured by classical lattice theory. The mechanistic underpinnings for their strength are

425 complex and are a subject of current research. Hollow lattices are often observed to have a

426 weaker strength than that predicted by Equation 1, and this is primarily attributed to localized

427 bending of the hollow nodes. Strength is limited by the "weakest link", so bending of hollow

428 nodes may not have much effect on lattices with a bending-dominated topology, as is the case

429 for hollow-beam nickel lattices made by SPPW[15], whose effective strength scaling is well

430 described by Equation 1. However, hollow node bending can have a drastic effect on the

431 strength of stretching-dominated topologies. Also, high sensitivity to processing-related

432 imperfections such as waviness and non-ideal beam cross-sections has been discussed.[13,16,19,82]

433 The linear strength scaling observed in rigid micro- and nanolattices at low $\bar{\rho}$ is up to 10 times

434 lower than the strength predicted by theory (Figure 4b); using Equation 1 to estimate the

435 constituent solid material strength (σ_s) of hollow-beam alumina lattices results in values of

436 $\sigma_s \approx E_s/300$ (Figure 4b), despite values of $\sigma_s \approx E_s/30$ having been found for single lattice

437 elements[107].

438 Shape optimization of lattice nodes may have the potential to improve the strength in particular

439 of hollow-beam and core-shell nanolattices. In core-shell lattice materials, stress concentrations

440 were shown to increase dramatically with an increasing stiffness gradient between the core and

441 shell, with the extreme case being a hollow shell[3,87]. For polymer-alumina core-shell lattices,

442 stress concentrations were also shown to cause substantial knockdown of the tensile strength

443 with respect to the compressive strength.[87] Hollow "shellular" lattices[108], namely lattices

444 without struts that consist only of smooth interconnected nodes, were developed with the aim

445 to reduce stress concentrations. Despite their optimized node shape, they have a fairly low

446   geometric parameter, C, and a high sensitivity to shell buckling instabilities, though, and show

447   little improvement in strength with respect to non-shape-optimized hollow-beam octet

448   lattices.[108,109]

449   *2.1.3. Size Effects and Strength*

450   When the length scale of architecture of a cellular material is small enough to fully exploit size-

451   dependent strengthening, its effective strength may be on the order of 30 times higher than that

452   of self-similar macroscale materials. A brittle perfect crystal reaches the theoretical strength

453   (σ_{th}) when the atomic bonds of two adjacent atomic layers break simultaneously. Based on an

454   equilibrium analysis of the work required to cleave the crystal and the energy released in the

455   formation of the new surfaces, σ_{th} has been estimated to be on the order of $E_s/10$.[102] For ideal

456   ductile materials, a theoretical strength of $E_s/30$ has been derived based on a shear failure

457   criterion.[102] In practice, the synthesis of monolithic bulk materials involves the introduction of

458   imperfections such as dislocations, grain boundaries, voids and cracks, all of which give rise to

459   typical bulk strengths of metals and ceramics on the order of $E_s/300$. The relative strength-

460   density property chart in Figure 5c illustrates the cellular material bounds for different ratios of

461   σ_s to E_s.

462   The strength of a material depends on the characteristic intrinsic size, i.e. the length scale of its

463   microstructure meaning the size and distribution of its flaws. Corresponding to Griffith's law[28],

464   the fracture strength (σ_f) of brittle materials increases as

465    $$\sigma_f = Y \frac{K_{Ic}}{\sqrt{\pi a_c}} \tag{4}$$

466   when the critical size of a crack (a_c) is reduced.[102] The fracture toughness (K_{Ic}) quantifies a

467   material's resistance to crack growth, and Y is a non-dimensional geometric parameter. In bulk

468   technical ceramics, the size of cracks is typically on the microscale or larger, resulting in

469   characteristically low fracture strengths[51]. The yield strength (σ_y) of ductile metals is generally

470   governed by the presence of obstacles to dislocation motion and may be described by

471    $\sigma_y = \sigma_0 + \dfrac{k}{l^n}$ (5)

472   where σ_0 usually is the bulk strength and k and n are constants.[30] The characteristic length (l)

473   traditionally represents the size of grains or particles or the spacing between dislocations. When

474   l is taken to be the grain size, Equation 5 is known as the Hall-Petch relation[110,111], which

475   describes strengthening in polycrystals with decreasing grain size. In this equation, $n = 1/2$

476   and σ_0 is an estimate of the strength of a single crystal (for $l \to \infty$). Strengthening mechanisms

477   like the Hall-Petch relation are well established, although the grain sizes of bulk metals are

478   typically above the nanoscale.

479   Ultimately the intrinsic size of a material is limited by its extrinsic size, i.e. its characteristic

480   dimensions (d_i). As the size of a material approaches the nanoscale, this finiteness becomes

481   "feelable" and it can be assumed that intrinsic features are on the same length scale as extrinsic

482   ones, i.e. a_c , $l \propto d_i$.This leads to the well-known "smaller is stronger" phenomenon[27,29–31],

483   where strength have been found that far exceed bulk values. There is no universal scaling law

484   for size-affected material strengthening as it arises due to the complex interaction of a number

485   of different intrinsic and extrinsic mechanisms. Yet based on relations like those in Equations

486   4 and 5, the strength of both brittle and ductile solids (σ_s) is often estimated to increase as

487    $\sigma_s \propto \left(\dfrac{1}{d_i}\right)^n$ (6)

488   at small scales (Figure 5b), where n generally is in the range of 0.5-1[29,30].

489   Below a certain critical dimension (d_i^*), which is typically in the range of 1-100 nm, σ_s can

490   reach values as high as the theoretical strength. Theoretical strength has repeatedly been

491   demonstrated with single crystalline ceramic and metallic specimens[37], where the confined

492   extrinsic sizes result in a near ideal material. Flaw insensitivity has also been discussed for

493   length scales below d_i^*.[29] According to Equation 4, the stress needed to fracture a brittle

494   material with a critical crack length smaller than $a_c^* \propto d_i^*$ would exceed the theoretical strength.

495   Notch insensitivity in ductile single crystalline gold nanowires has been shown to result from

496   strain hardening.[48] No polycrystalline metals have been found that reach σ_{th}, and the critical

497   dimension relates instead to the peak strength of the grain boundaries.[27,31,112] When dislocation

498   loops no longer fit inside grains, grain boundary strengthening breaks down.[27] In size ranges

499   below d_i^*, mechanisms such as sliding of grains at the free surfaces can induce a weakening

500   effect.[27,31,113]

501   In a lattice, the characteristic dimension (d_i) may be the beam diameter or the wall thickness of

502   an individual lattice element, which in a nanolattice may be designed as small as the critical

503   dimension (d_i^*). This mechanism allows nanolattice materials to substantially exceed the limits

504   of macroscale cellular materials, as Figure 4b and Figure 5c show. By contrast, self-similar

505   macrolattices with $d_i \gg d_i^*$ cannot benefit from the size-affected strengthening in Equation 6.

506   Pyrolytically derived ceramic nanolattices exploit material strengths on the order of the

507   theoretical strength. Figure 5c shows that the effective strength of the glassy carbon

508   honeycombs[1] and the nanolattices with $\bar{\rho} \approx 25\%$[1] reach the cellular-materials' bounds for

509   stretching-dominated behavior corresponding to $\sigma_s = E_s/10$ with $E_s = 28$ GPa[99]. High purity

510   of the starting resin results in a low population of flaws after the material is transformed into a

511   ceramic.[84] Polymer resin-derived SiOC lattices and honeycombs with macroscale dimensions

512   already achieve remarkable strength, and when the dimensions are reduced, the flaw sizes

513   decrease correspondingly. For a solid-beam lattice, a surface crack along the diameter of a strut

514   may be a critical strength-limiting flaw. If a fracture strength of $\sigma_f = E_s/10$ is used, Equation 4

515   gives a critical flaw size of $a_c \approx 30$ nm for glassy carbon with $E_s = 28$ GPa[99],

516     $K_{Ic} = 0.91$ MPam$^{0.5}$[114], and $Y = 1$[115]. The strut diameters of the glassy carbon nanolattices are

517   in the range of 200 nm, flaws are likely to be much smaller than 30 nm, and based on Equation 4

518   it is reasonable to expect corresponding material strengths of $E_s/10$.

519   Atomic layer deposited hollow-beam ceramic and core-shell composite nanolattices notably

520   benefit from material strengthening size effects, but they may not make full use of them in their

521   effective properties. In agreement with Equation 6 with $n = 0.5$, tensile experiments on

522   polymer-alumina composite lattice elements[107] and bulge tests on suspended alumina

523   membranes[100] showed that the strength of ALD alumina shells increases up to 5.5 GPa when

524   their thickness is reduced below 50 nm. The theoretical strength of these materials has not been

525   reached, a fact that may be attributed to the porosity of atomic layer deposited ceramics, which

526   is as also reflected in their reduced density[116] and Young's modulus[100] compared to the

527   corresponding bulk material. Although strengths of 5.5 GPa are below the theoretical limit, they

528   are as much as 20 times higher than the corresponding bulk strength[51,117]. As described in

529   Section 2.1.2, strength gains in hollow-beam and core-shell composite lattices are often not

530   fully reflected in their effective strength due to their shell-based designs and their sensitivity to

531   structural imperfections. The constituent material strength of sintered particle-based lattices[19]

532   is limited by their high flaw population, which may be rather independent of the length scale.

533   Single crystalline metallic nanolattices achieve material strengths in the range of the theoretical

534   shear strength. Interpolating the measured effective strength of the nickel gyroids[9] to that of

535   the fully dense material gives $\sigma_s = E_s/30$ with $E_s = 214$ GPa[51] (Figure 5c). Nickel gyroid films

536   have a columnar polycrystalline structure with in-plane grain sizes of about 1.5 μm. However,

537   their constituent unit cell sizes of 45 nm enable strengths on the order of single crystalline nickel.

538   Nanoscale single crystalline metal specimens approach theoretical strengths via mechanisms

539   such as dislocation starvation, wherein dislocations exit at free surfaces and leave behind a

540   dislocation-free material.[31] The critical dimension of face-centered cubic nickel can be

541   estimated to be 13nm using Equation 5 with k estimated from the Burger's vector and the shear

542 modulus and $n = 0.66$[118]; this matches the strut diameter of the nickel gyroids.[9] Similar

543 relations can be found for nanoporous gold foams, whose effective strength has been described

544 over a feature length scale range of 10-900 nm by replacing σ_s in Equation 1 with

545 Equation 5;[94] comparable systematic studies have not yet been performed for nanolattices.

546 The benefit of small-scale structuring may be limited in lattices made from polycrystalline

547 metals. The strength of electroless deposited nanocrystalline nickel-based thin films, similar to

548 those used in some hollow-beam microlattices[15,19,83], has been estimated to be ~2 GPa based

549 on hardness measurements.[19,101] While this strength is higher than many bulk nickel alloys,

550 strengths of 4.3 GPa have been found in amorphous metal films of core-shell composite

551 lattices[88]. Compression tests of 7 nm-grained hollow-beam lattice elements showed a drastic

552 decrease in strength when wall thicknesses were reduced from 500 nm to 150 nm, the

553 magnitude of which could not be explained by geometry alone and was also attributed to the

554 "smaller is weaker" effect that is induced by the sliding of grains at the free surfaces.[101] A

555 similar behavior may explain the drop in strength of hollow-beam nickel octet microlattices[19]

556 shown in Figure 4. As dimensions are reduced, the fraction of grains at the free surfaces

557 increases, intensifying surface sliding weakening effects. This is distinctly reflected in low-

558 strength hollow-beam gold lattices synthesized via sputtering[90], which have grain sizes of 25-

559 50 nm and feature dimensions down to 200 nm. Copper microlattices with strut diameters in

560 the range of 1-3 μm mostly consist of grains spanning entire lattice members[89]. They are

561 therefore neither fully single- nor polycrystalline, and corresponding strengthening and

562 weakening effects may be present at the same time. The constituent material strengths of copper

563 microlattices can be estimated to be on the order of $E_s/300$. However, their effective strength

564 has been shown to be three times higher than the strength of 10 μm thick polycrystalline copper

565 films synthesized under identical conditions.[89]

566 **2.2. Stiffness**

567 In quantifying the performance of lightweight materials, the specific stiffness, or the ratio

568 between Young's modulus and density, is as important as the specific strength. Lattice stiffness

569 depends on architecture, and topologies that are optimized for high strength generally achieve

570 high stiffness. In contrast to strength, reducing the length scale of lattice architectures has not

571 been shown to lead to any size-affected increase in the stiffness of the constituent materials.

572 Size-effects in the stiffness are still a subject of current research and may be limited to a small

573 number of materials, such as carbon[43–47]. Taking advantage of stiffness size effects in

574 nanolattices may require a further decrease in feature sizes beyond what is achievable today.

575 Despite a lack of size-affected benefit to their constituent stiffness, micro- and nanolattices have

576 pioneered new regimes of stiffness versus density material property space. **Figure 6** compares

577 different nano-, micro- and macrolattices, stochastic nanoporous foams and commercial bulk

578 materials. Rigid architectures of hollow-beam alumina[13,19,82] and nickel-based[19] nano- and

579 microoolattices populate the ultra-light density "white space" below 0.01 g/cm³. These materials

580 have specific stiffnesses that do not considerably degrade over several orders of magnitude

581 decrease in density. As a result, they substantially outperform non-rigid lattices of the same

582 density and are demonstrably less dense than stochastic cellular materials of comparable

583 stiffness. Ultralight micro- and nanolattices achieve new material property spaces for both

584 stiffness and strength, but in higher density regimes of 0.1-1 g/cm³, the stiffness of nanolattices

585 does not reach the same "white space" that is reached for strength[1–3,14]. This illustrates the

586 beneficial impact of size-effects on nanolattice strength and its corresponding absence in the

587 stiffness.
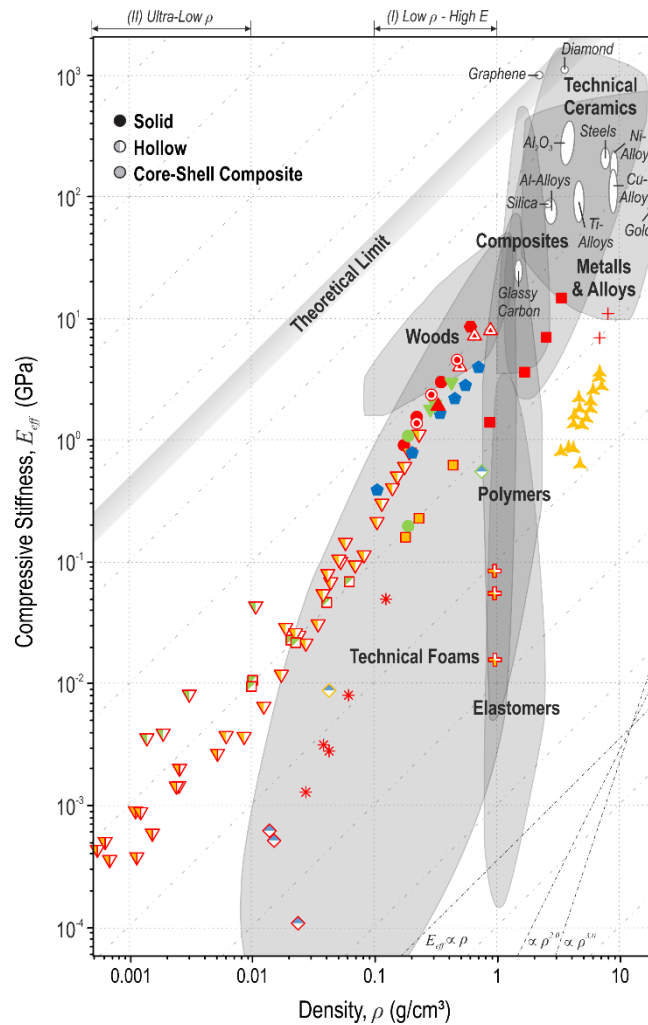
Figure 6. Compressive stiffness vs. density materials property chart comparing different nano-, micro-, and macrolattices as well as stochastic nanoporous and commercial bulk materials. Certain hollow-beam micro- and nanolattices reach far into the chart's ultralow-ρ "white space". For graphene[44] the tensile stiffness is shown. See Figure 4 for data point legend.

Analogously to the strength, the effective stiffness of cellular materials (E_{eff}) versus relative density is classically modeled by the relationship

$$E_{eff} = F\bar{\rho}^{g}E_{s} \tag{7}$$

where E_{s} is the constituent solid material's Young's modulus, F is a geometric parameter, and $g = 1$ and 2 are the exponents for ideal stretching- and bending-dominated behavior respectively. The impact of bending on the stiffness is more pronounced than it is for the strength, which has a scaling exponent of $a = 1.5$ for bending-dominated behavior. In the ultra-light density regime, stochastic materials can have scaling exponents of $g = 3$.[119] Geometric

27

602 parameters for open-cell foams of $F \approx 1$ have been found[51], and for the octet lattice, $F =$

603 $1/9 - 1/5$ has been predicted mathematically[52] depending on the loading direction. As is the

604 case for the strength, anisotropy can lead to increased stiffness in a preferred loading direction

605 but at the cost of decreased stiffness in other directions.

606 It can be seen in Figure 6 that the stiffness of many of the lattice materials does not scale

607 perfectly linear or quadratic with the density, but instead falls somewhere in between. This

608 occurs because the relationship defined in Equation 7 is only valid for lattices with slender

609 beams. Equation 7 provides a useful guideline for quantifying the performance of a given

610 topology, but it likely obscures some of the more complex mechanical phenomena observed in

611 actual lattices, particularly in those made from hollow beams or shells. The stiffness of lattices

612 can also be affected by structural defects like the removal of strut members, stress

613 concentrations at nodes, local shearing and bending in strut members, and waviness or

614 misalignment of the struts;[13,19] investigations into these effects are a topic of ongoing research.

2.3. Recoverability, Energy Absorption & Damage Tolerance

616 The deformability of materials can be greatly enhanced through the addition of architecture.

617 Micro- and nanolattices are able to take intrinsically brittle and low elastic limit materials – like

618 ceramics and certain classes of metals – and use them to create metamaterials that are able to

619 undergo large deformations of up to 80% compressive strain without catastrophic

620 failure.[13,15,18,82,83] This is primarily enabled by scale-independent architectures that deform in

621 ways that accommodate large displacements and in part because of nanoscale constituent

622 materials that can withstand larger elastic strains due to increased yield strengths. Enhancing

623 the deformability gives rise to three important architected material properties: recoverability,

624 energy absorption, and damage tolerance.

625 Hollow-beam micro-[15,18] and nanolattices[13,82] made from both ductile and brittle constituent

626 materials have demonstrated near 100% recoverability after compression to 50% strain (**Figure**

627 **7)**. A transition from brittle failure to recoverable deformation was observed below a certain

628 critical wall-thickness-to-strut-diameter ratio (*t/D*). This phenomenon was attributed to shell

629 buckling of thin-walled struts, which can form low stress hinges that prevent catastrophic failure

630 and accommodate large macroscopic reversible strain.[13,17,18] Recoverability has been shown

631 with both rigid and non-rigid topologies, but relative densities are generally required to be very

632 low to enable shell buckling.
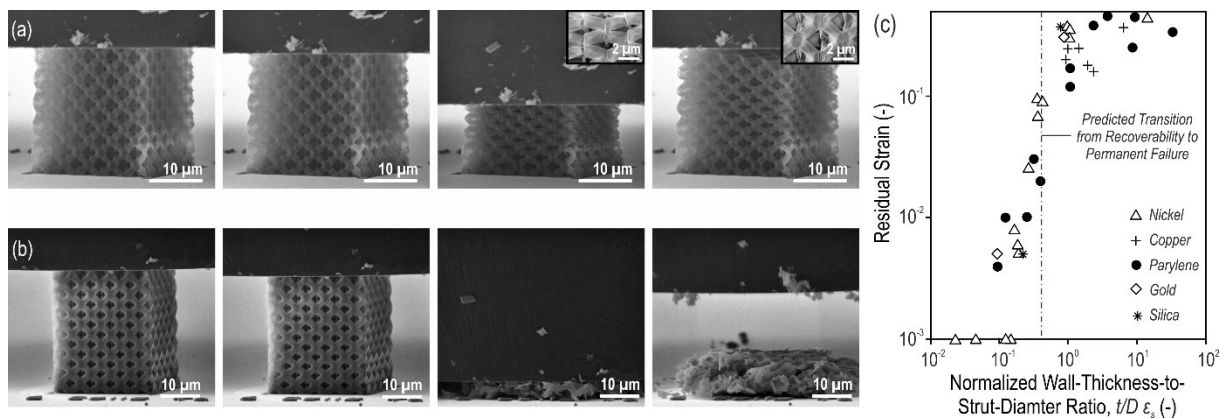
633

634 **Figure 7. Recoverability of micro- and nanolattices.** (a) Compression of thin-walled and (b)
635 thick-walled hollow-beam alumina nanolattices, demonstrating the effect of shell buckling on
636 increasing the deformability and recoverability of intrinsically brittle materials. (c) Residual
637 strain of hollow-beam microlattices fabricated via SPPW, after 50% compression vs. wall-
638 thickness-to-strut-diameter ratio (**t/D**) normalized by the yield strain of the constituent material.
639 The critical ratio **t/D** that guarantees full recoverability from any imposed macroscopic strain
640 can be estimated analytically. Adopted from [18] and reproduced with permission, [13] 2014, The
641 American Assosiation for the Advancement of Science.

642 Controlling the activation of different failure mechanisms is key to enabling the enhanced

643 deformability observed in nano- and microlattice materials. In a lattice the primary failure

644 mechanisms are constituent material failure, beam buckling, and shell buckling in lattices with

645 hollow members. The strength of the solid material (σ_s) is an intrinsic material property, but it

646 can be greatly affected by feature size, as is discussed in Section 2.1.3. The beam buckling

647 strength was defined in Section 2.1.2 for slender beams using the Euler buckling criterion of

648 $\sigma_{eb} = k^2\pi^2 I E_s/(Al^2)$. The shell buckling strength for hollow circular beams is $\sigma_{sb} =$

649    $E_s(t/R)/\sqrt{3(1-v^2)}$, where t is the wall thickness, R is the beam radius, and v is the

650   constituent material Poisson's ratio.[120]

651   The failure mechanism that governs the initiation of failure can be determined by setting these

652   three equations equal. The critical transitions ratios between material failure and beam buckling,

653   material failure and shell buckling, and beam and shell buckling for a thin walled hollow

654   circular beam respectively are

655
$$\left(\frac{R}{l}\right)_{s\rightarrow eb} = \frac{1}{\pi}\sqrt{\frac{\sigma_s}{2E_s}}$$

656
$$\left(\frac{t}{R}\right)_{s\rightarrow sb} = \frac{\sigma_s}{E_s}\sqrt{3(1-v^2)}$$

657
$$\left(\frac{tl^2}{R^3}\right)_{sb\rightarrow eb} = 2\pi^2\sqrt{3(1-v^2)}$$

658   Using these relationships as guidelines, architected materials can be designed to undergo failure

659   via one of these mechanisms using any constituent material.

660   Buckling is the cornerstone of much of the deformability, recoverability and energy absorption

661   observed in micro- and nanolattices. It is an intrinsically elastic phenomenon, meaning that if

662   the stress in a post-buckled beam doesn't reach the yield or fracture strength of the material, a

663   structure will be able to recover to its original shape. This recovery can occur independently of

664   architecture, and lattices can simultaneously be designed to be recoverable and to have high

665   strength and stiffness.

666   In lattices with beam buckling dominated failure, beams must be highly slender and nodes must

667   either be reinforced or able to rotate in order to ensure post-failure recoverability. Node

668   reinforcement, such as selectively increasing the material thickness at the node, can be done in

669   any architecture, but node rotation is best enabled in architectures with non-rigid topologies

670   like octahedral-type unit cells[121], which have intrinsic mechanisms that allow for a greater

degree of deformation. In lattices with shell buckling dominated failure, shell walls must be thin and have large radii of curvature to improve structure recovery. In locally buckled sections of beams, a compliant hinge is formed that enables greater deformation.[13,55] Permanent failure can and does often occur in these locally buckled regions, but structures can still globally recover if the failure is unable to propagate to the rest of the beam. This behavior has been observed experimentally, but there is not a well-developed theory on how to design geometries that form buckled hinges that can impede brittle failure propagation.

The ability of a recovered structure to retain its initial strength and stiffness is crucial to its utility as an engineering material. Due to the activation of certain failure modes and the buildup of local damage, the post-yield stiffness and strength of a recovered structure is generally lower than that of the undeformed material.[15,55,82] Reducing the applied strain on a structure can help it to retain its strength, but it is difficult to completely preserve the initial mechanical properties. When repeatedly compressed to the same strain, structures often exhibit a stable cyclic behavior.[15,55,82] This occurs because failure modes that were activated in the initial cycle can be reactivated, minimizing the accumulation of additional damage.

Fracture, plastic work, and intrinsic material damping dissipate energy in continuum materials; in recoverable lattices, buckling and other hysteretic instabilities are the dominant mechanisms that cause energy dissipation. Beams that buckle often exhibit a bistable behavior, during deformation they undergo a snap-through between a buckled and unbuckled state. This snap-through event induces high-frequency vibrations which are eventually damped, resulting in energy dissipation. The character of the snap-through events can also be controlled by changing the type of buckling; for example, Euler buckled beams in uniaxial compression will maintain an approximately constant load, while shell buckled beams will have a drop in load carrying capacity in their post-buckled configuration.[122] In lattice architectures buckling and snap-through events can be coordinated to dissipate energy in a controlled manner, and structures

696 can be designed to enable layer-by-layer deformation, uniform crushing, or localized

697 failure.[13,82,83,123–126] One important characteristic damping parameter is the mechanical loss

698 coefficient, defined as $\eta = \Delta U / 2\pi U$, where U is the stored elastic strain energy and ΔU is the

699 dissipated strain energy.[127] It has been shown that that lattices can be designed to have

700 exceptionally high damping figures of merit $E^{1/3}\eta/\rho$.[55] Structures with optimized damping

701 will generally have low relative densities ($\bar{\rho} < 0.1\%$) and hence low strength and stiffness.

702 High density architected materials that dissipate energy via snap-through buckling of hinges

703 while maintaining recoverability have been proposed.[123–126]

704 When maximizing energy dissipation per unit mass, e.g. for the development of armor systems,

705 plastic flow is the mechanism of choice. Polymer and ceramic-polymer composite nanolattices

706 fabricated by interference lithography[62] were shown to dissipate exceptional amounts of

707 energy per unit mass.[128–131] This was attributed to the ability of the structure spread plastic

708 deformation over a large volume; in a bulk material, failure is generally localized to a single

709 shear band or necking region, whereas failure in lattices can occur homogeneously throughout

710 a sample. Although plastically deformable nanolattices possess exceptionally high specific

711 energy dissipation, their deformation is not recoverable and therefore not repeatable.

712 The design of damage tolerant and lightweight materials is still a major engineering challenge.

713 The fracture toughness of a periodic lattice scales with the square root of the unit cell size,

714 meaning that it decreases when the unit cell size is reduced.[49,132–134] For octet or hexagonal

715 lattices, a single "missing" beam introduces a stress concentration.[132,134] In contrast, Kagome

716 lattices are insensitive to flaws smaller than a certain transition length.[132,135] This transition

717 length scales with $1/\bar{\rho}$ and can be several times the unit cell size.[132] In nanolattices, material

718 strengthening size effects should counteract the size-dependent weakening of the

719 architecture.[134] Therefore, there may be a slight benefit to the toughness of nanolattices, but

720 the substantial design challenge remains. A possible solution might be in the use of hierarchical

721 designs, where larger unit cells could impart toughness while smaller nested unit cells would

722 be used to exploit size-dependent strengthening effects. Hierarchical micro- and nanolattices

723 have also been observed to have increased recovery beyond that of simple periodic lattices

724 because failure is localized to sections of hierarchical beams, allowing structures to undergo

725 permanent damage while still recovering globally.[82,83]

726 There are many other size-affected material properties like enhanced ductility[38,42], fatigue

727 resistance[136], and fracture toughness[29] that have been observed in nanomaterials but have not

728 been used in practical implementations. Future developments in nanoarchitected material

729 design may rely on these and other size affected material properties to push the limits of

730 mechanical performance.

731 **2.4. Auxetic Behavior**

732 The concept of auxetics[137], namely materials with negative Poisson's ratio, holds great promise

733 for adding new functionality to nanolattices. At the macroscale, auxetic structural designs are

734 progressively employed in the development of novel products, especially in the fields of

735 intelligent expandable actuators, shape morphing structures, and minimally invasive

736 implantable devices.[138] There is a wealth of possible auxetic designs, many of which rely on

737 folding and unfolding mechanisms of non-rigid topologies, and there are many possibilities for

738 the creation of three-dimensional architectures that achieve Poisson's ratios down to -1 or

739 lower.[139] Poisson's ratio of zero describes a material that retains its lateral dimensions upon

740 compression, while Poisson's ratio of -1 describes a material that will shrink laterally an equal

741 amount to what it is compressed vertically, thereby keeping its shape but not its volume.

742 Poisson's ratios of -0.8 have been demonstrated for macroscopic lattices, and a design for an

743 ideal dilational metamaterial with Poisson's ratio of -1 has been proposed.[67] Materials with

744 Poisson's ratios of -1 require infinitesimal joints to achieve their performance. The small

745 dimensions and enhanced material properties of nanolattices may be able to replicate such ideal

746   joints.[67] Auxetic lattices based on the bow-tie design were created **(Figure 8a-b)** exhibiting

747   different Poisson's ratios depending on the precise shape of their bow-tie elements.[20] In these

748   materials, subtle design changes were used to shift Poisson's ratio from negative to zero or even

749   positive values. Applying thin alumina coatings using atomic layer deposition to the polymer

750   structures increased the stiffness while leaving Poisson's ratio unaffected. With the ever

751   increasing precision in manufacturing capabilities, progressive size reduction of auxetic

752   geometries may allow the exploitation of mechanical size effects in nanolattice materials with

753   tailorable adaptivity.[140]
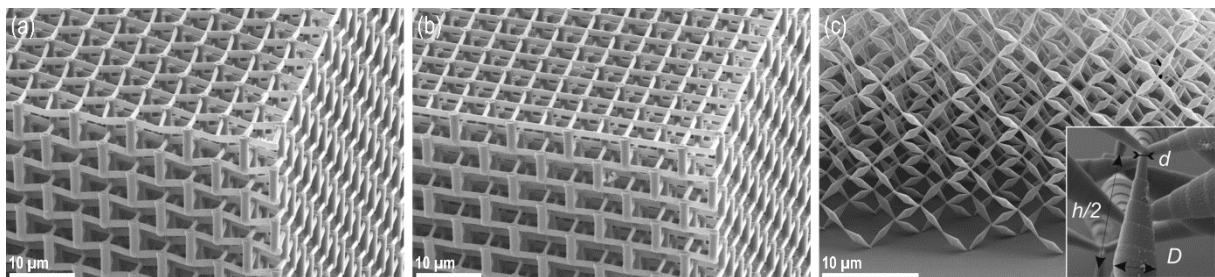
754

755 **Figure 8. Nanolattices achieving extreme tunable mechanical properties.** (a-b) Auxetic
756 lattices based on the bow-tie design with four-fold symmetry, subtle structural variation
757 changes Poisson's ratio from (a) -0.14 to (b) 0.01. (c) Pentamode lattices have a very large bulk
758 modulus compared to the shear modulus. Ideally, the connecting points of the double-cones
759 would be infinitely small and control the modulus ratio. Minimum cone diameters d of 550 nm
760 were achieved. By increasing the cone diameter D, the mass density of the lattice can be
761 adjusted. Reproduced with permission, [20] 2012, John Wiley and Sons, [21] 2012, AIP
762 Publishing LLC.

763 **2.5. Metafluidic Behavior**

764   Pentamode metamaterials, also referred to as metafluids, have a very large bulk modulus

765   compared to their shear modulus, which ideally is zero. A material with a very large bulk

766   modulus will have little volume change during deformation, meaning its Poisson's ratio is close

767   to 0.5.[21] A material with a very small shear modulus will "flow away" under shear in a manner

768   similar to a fluid.[21] Pentamode metamaterials combine these two principles to generate an

769   elasticity tensor with only one non-zero eigenvalue and five eigenvalues that are negligibly

770   small.[60] Based on a concept by Milton and Cherkaev[141], these materials can be created using

771   rigid, double-cone elements connected to each other at their point-like tips and arranged in a

772   diamond-type lattice (Figure 8c).[21] Actual structures are approximations of the ideal

773   pentamode material having zero diameter of the cone ends, but minimum cone tip diameters of

774   550 nm have been achieved, resulting in bulk-to-shear modulus ratios of approximately

775   1000.[21] The bulk modulus of such a double-cone lattice is mainly determined by the diameter

776   of the cone tip; increasing the cone diameter will primarily affect the mass density of the lattice

777   and has less significance for the modulus.[142] If minimum cone diameters smaller than 550 nm

778   were achieved, a further enhancement of the bulk-to-shear modulus ratio should be possible,

779   which would facilitate the fabrication of three-dimensional transformation-elastodynamic

780   architectures[21,143] like free-space cloaks that render objects invisible to incident radiation. For

781   elastomechanical cloaking, macroscale pentamode lattices with different modulus ratios were

782   combined to render a physical object "unfeelable".[144] The concept of reducing the dimensions

783   of the connection points in a lattice was applied to design nanolattices with maximized

784   anisotropy of the elastic modulus.[145] These face-centered cubic nanolattices were created using

785   interference lithography and achieved an elastic-to-shear-modulus-ratio of four.

786   **2.6. Non-Mechanical Properties & Multifunctionality**

787   *Photonic metamaterials*[62–64] are micro- or nanoarchitected to enable interaction with

788   electromagnetic waves such as visible light (wavelength 400-700 nm). Notable examples

789   include silicon woodpile lattices with engineered defects exhibiting near-infrared complete

790   photonic bandgaps, chiral and bi-chiral polymeric photonic crystals featuring polarization

791   stopbands, photonic quasicrystals, and polymeric woodpile lattices with spatially tailored

792   density, providing invisibility cloaking at optical wavelengths[22,23]. The development of

793   tailored photoresists for multi-photon lithography and multi-laser polymerization approaches

794   based on stimulated emission depletion (STED) achieve significantly increased resolution,[146–

795   148] further enhancing the opportunity to design nanolattices with unique optical properties.

796 *Phononic metamaterials*[62,65,66] are designed to interact with mechanical waves. Mechanical

797 waves travel within a homogeneous and isotropic medium with the dispersion relation $\omega = c \cdot$

798 k, where ω is the frequency, k is the wave vector and c is the velocity of propagation in

799 longitudinal or shear direction. If the medium has an intrinsic periodicity, though, a much more

800 complex dispersion relation results, with several acoustic and optical branches. When properly

801 designed, the periodic medium might exhibit "band gaps", i.e. ranges of frequency where wave

802 propagation is prohibited along any direction. Acoustic metamaterials with unit cells in the

803 centimeter range have been developed extensively.[149] Recently, DLW has been employed to

804 fabricate phononic crystal at the microscale, which can tailor ultrasonic wave propagation.[150]

805 Phonons (thermal vibration within the atomic lattice) are largely responsible for heat conduction

806 in non-metallic solids. In principle, nano-architected materials could be designed to interact

807 destructively with phonons, possibly resulting in exceptionally low thermal conductivity; the

808 key challenge is that phonons responsible for heat conduction have extremely low wave length,

809 and hence can only interact with architected materials with periodicity on the order of ~1 nm.[66]

810 Cellular materials have been exploited for *thermal management* for decades.[51,151] When

811 fabricated in ceramic constituent at very low density, they provide exceptionally low thermal

812 conductivity and diffusivity; conversely, when fabricated in metal with open porosity, they

813 enable active cooling and efficient heat transfer from the hot to the cold side.[152] Optimized

814 lattice architectures such as multi-scale heat pipe structures[153] substantially improve thermal

815 properties compared to stochastic foams.[154] In all these applications, length scale reduction

816 promises performance improvements, thanks to size effects in the thermal

817 conductivity[32,33].[155]

818 Lattice materials with *tunable thermal expansion* can be designed by properly combining

819 different constituent materials, or folding mechanisms similar to those of auxetic structures. A

820 number of possible designs have been proposed and demonstrated at the macroscale.[56,156–158]

821   If fabricated at smaller scale, these multi-constituent architected materials would be useful for

822   applications where dimensional accuracy is essential under continuous temperature excursions,

823   e.g. positioning of micromirrors[159] in space applications. Recently, multimaterial PµSL has

824   been used to develop a bi-material negative Coefficient of Thermal Expansion polymeric lattice

825   with unit cell size of ~5mm.[160] In the context of thermal size effects, the ability to generate

826   similar multi-material topologies with dimension reduced by several orders of magnitude may

827   hold opportunities for novel applications.

828   *Electrochemical phenomena* such as upon lithiation/delithiation of electrodes for advanced

829   lithium ion batteries require very large surface area, interconnected porosity, and the ability to

830   accommodate strains, up to several hundred percent, without mechanical failure. The ability to

831   optimize the topology of a nanolattice can dramatically improve the combination of transport,

832   electrochemical and mechanical properties over that of state-of-the-art stochastic porous

833   materials. Self-assembly has been applied to develop energy storage and conversion devices

834   such as solar cells, batteries, and fuel cells.[161] Glassy carbon[162] and copper-silicon[163]

835   nanolattices fabricated by interference lithography and DLW, respectively, were proposed as

836   electrode materials. Although not quite a nanolattice, pillared graphene nanostructures have

837   been shown to possess excellent specific capacitance and coulombic efficiency which are ideal

838   properties for supercapacitors.[164]

839   In *bio-technology*, micro- and nanolattices with controlled three-dimensional architecture have

840   been successfully used for tissue engineering,[165] as scaffolds for controlled cell cultures,[166]

841   and in minimally invasive medicine[167]. Chemical functionalization, as demonstrated with

842   polymeric lattices generated using DLW, with pre-functionalized photomonomers[168]

843   potentially qualifies nanolattices for a variety of biomedical and biochemical applications.

844   **3. Fabrication**

845 Lattice structures with millimeter to centimeter scale periodicity can be efficiently fabricated

846 via the assembly of folded and/or slotted thin sheets (similar to a cardboard box), or by modular

847 assembly methods such as wire layup.[169] Additive manufacturing (AM) technologies[170] like

848 selective laser sintering, selective laser melting, stereolithography and electron beam melting

849 offer sub-millimeter resolution and increased design freedom, but at the cost of a lower

850 production rate. The production rate of a manufacturing process generally scales inversely with

851 its accuracy and resolution capacity. Fabrication techniques with micrometer and nanometer

852 resolution, such as those required for fabricating nanolattices, are currently limited to a number

853 of polymer-based, low throughput, AM and self-assembly techniques. Those that have been

854 most successfully applied to micro- and nanolattice fabrication are described in the following

855 sections. We discuss the achievable resolution, productivity and design freedom, and give an

856 overview on the most commonly used methods to convert polymeric structures into ceramic,

857 metallic and composite lattices.

3.1. Self-Propagating Photopolymer Waveguides (SPPW)

859 SPPW is an angled exposure technique to fabricate open-cell polymer structures from self-

860 propagating photopolymer waveguides.[4,121] With this technique, exposes a photomonomer by

861 ultraviolet (UV) light passed through a two-dimensional mask with a pattern of apertures as

862 shown in **Figure 9a**. In the photomonomer, self-propagating photopolymer waveguides

863 develop at each aperture in the direction of the UV collimated beam and cross at points of

864 intersection, forming a three-dimensional interconnected array of polymer struts. After

865 removing the uncured monomer, an open-cell polymer material is left behind. SPPW controls

866 the architectural features of the bulk cellular material by controlling the strut angle, diameter,

867 and three-dimensional spatial location during fabrication. The unit cell architecture is governed

868 by the pattern of circular apertures on the mask and the orientation and angle on the collimated

869 incident UV light beams. With standard UV exposure capabilities, lattices have been fabricated

870   with strut diameters ranging from ~10 μm to >1 mm and a relative densities between ~5 % and

871   30%. The overall material thicknesses can range from 100 μm to over 25 mm per exposure. The

872   maximum achievable material thickness, which is dependent on the distance the waveguide can

873   propagate, is roughly 100 times the lattice member diameter. To achieve higher thicknesses,

874   multiple layers have to be exposed similar to other layer-by-layer AM techniques. The lattice

875   strut angle relative to the exposure plane can be between ~50° to 65° for directly intersecting

876   waveguides. Vertical or near vertical struts are also producible. Changing the aperture spacing

877   and diameter on the mask enables variations in the lattice feature dimensions and unit cell sizes

878   (Figure 9a). SPPW can only be used to fabricate architectures that are linear extensions of the

879   mask; this allows a range of non-rigid lattice truss topologies and honeycombs, but prohibits

880   rigid lattice topologies with struts parallel to the mask plane. Masks with larger apertures can

881   be used to make negative templates for shellular topologies that are rigid and don't contain in-

882   plane elements.[108] The main advantage of SPPW compared to other high resolution AM

883   approaches is the substantially higher speed and scalability. 30 cm x 30 cm x 20 mm polymer

884   lattices have been fabricated in 1 minute, and rates of more than 1 m^2/min are achievable with

885   a continuous SPPW process. Interference lithography[62] and other angled exposure techniques

886   such as x-ray lithography can be used to create similar topologies to those made using SPPW

887   and with feature diameters below 100 nm, albeit at the cost of considerably lower

888   scalability.[130] Multi-beam interference lithography markedly extends the variety of topologies

889   that can be created.[62] A range of resin systems are available for SPPW that enable lattices from

890   stiff,[121] viscoelastic,[171] or pre-ceramic[84] polymers.

3.2. Projection Micro-Stereolithography (PμSL)

892   Projection micro-stereolithography a layer-by-layer process for the fabrication of three-

893   dimensional polymer microstructures (Figure 9b).[5] For each layer, a reconfigurable digital

894   mask and a UV light-emitting diode (LED) array project an image onto the surface of a liquid

895 photomonomer bath, inducing polymerization in the shape of the projected image. The

896 thickness of the resulting layer is in the range of 10-100 μm, depending on the penetration depth

897 of the light, which is controlled by process parameters including light intensity[5,172,173],

898 exposure time[172,174], and the concentration of photoabsorber[175,176] and photoinitiator[177] in

899 the photomonomer. Lowering the polymerized layer into the resin bath forms a new liquid layer

900 on top of the polymerized layer and the process is repeated until the desired object is completed.

901 The spatial light modulator (SLM), which is usually a deformable mirror array (DMD),

902 combined with projection optics defines the resolution and scalability. For example, a typical

903 SLM with 1920 × 1080 pixels projected over an area of 15.36 mm x 8.64 mm combined with

904 UV reduction optics with a reduction factor of 6:1 gives a final resolution of 1.3 μm/pixel at the

905 projection focal plane. Three-dimensional lattices with feature sizes of 5 μm and 300 μm can

906 be fabricated in areas of 1 mm and 5 cm in 1 to 2 hours, respectively. Further extending the

907 scalability, Large Area PμSL[83] combines an addressable SLM with a galvanometric mirror

908 scanning system to produce microscale architectures over a large area. As the light is scanned,

909 the image projected from the SLM changes corresponding to the respective location of the

910 pattern. Hierarchical lattice materials with over 60,000 octet unit cells and with feature sizes

911 <5 μm (see Section 4) can be fabricated with a speed of 1,200 mm³/hour. The main advantage

912 of PμSL compared to high resolution AM techniques such as DLW is the increased fabrication

913 speed, which, due to the projection technique, is not compromised as feature complexity

914 increases. PμSL can work with a range of resins with inorganic nanoparticles[178,179], pre-

915 ceramic polymers[180–182], as well as resins with different colors[183], stiffness[184], and

916 viscosities[185]. Multi-material PμSL with feature sizes in the millimeter range has also been

917 shown.[160]

918 **3.3. Direct Laser Writing (DLW)**

919   Direct laser writing (DLW) is a multi-photon lithography process that facilitates the fabrication

920   of fully three-dimensional polymeric micro- and nano-structures (Figure 9c).[6,7] In DLW, an

921   optical microscope focuses a laser beam with a wavelength (λ) of typically 780 nm into a

922   volume of liquid photoresist. The photoresist contains a photoinitiator that absorbs the laser

923   light and causes polymerization of its monomers. The photoinitiator is transparent to light with

924   a wavelength λ but absorbs light at $\lambda/2$, which has double the energy than light at λ. If two or

925   more photons of wavelength λ are absorbed simultaneously, the sum of their energy is high

926   enough to induce polymerization. This is known as multi-photon absorption, which is a second-

927   order process that is several orders of magnitude weaker than the single-photon absorption used

928   in SPPW or PμSL. In the DLW process, multi-photon polymerization is achieved by focusing

929   of the laser light. As the absorption reaction depends on the square of the light intensity there

930   is no polymerization along the path of the light but only in a small focus volume. The result is

931   an ellipsoidal polymerized voxel, or volume pixel, that is typically >200 nm wide and >600 nm

932   high.[148] DLW with resolutions down to 100 nm have been achieved using more complex

933   optical configurations.[148,186] By moving the laser focus sample one can "write" three-

934   dimensional structures into the photoresist. Piezoelectric xzy-stages with nanometer accuracy

935   can move the sample in all directions at speeds of tens of micrometers per second. Galvo mirrors

936   enable rapid in-plane scanning of the laser focus with a scan speed of up to m/s. In practice,

937   both writing methods are combined to achieve typical writing speeds on the order of mm/s. The

938   working area of both writing methods is generally limited to a few hundred micrometers, the

939   fabrication of larger structures requires stitching of multiple writing fields. A range of

940   positive[24] and negative[64,166,168,187,188] tone photoresists can be used in fabricating

941   nanolattices.[189] After samples are written, the remaining photomonomer is dissolved in a

942   developing bath, leaving the finished structure behind. Super critical drying[190] can be applied

943   during the development stage to avoid distortion of the structure due to capillary effects. DLW

944   has the highest achievable resolution of any fully three-dimensional AM technique, and it is

945 therefore the method of choice for the fabrication of nanolattices. The main challenge DLW

946 faces is its scalability; the size of fabricated samples typically ranges from hundreds of

947 micrometers to centimeters depending on the complexity of the structures being written.

3.4. Self-Assembly

949 Self-assembly based approaches have shown great promise for the fabrication of complex

950 micro- and nanostructures, and are therefore often seen as an alternative to additive

951 manufacturing. As defined by Whitesides and Grzybowski, "Self-assembly is the autonomous

952 organization of components into patterns or structures without human intervention"; this

953 process is applicable at all length scales, although the first studies focused on the self-assembly

954 of molecules.[191]

955 Block copolymer self-assembly (Figure 9d) has been successfully used in the fabrication of a

956 variety of periodic functional nanostructures with dimensions on the order of tens of

957 nanometers.[192,193] Block copolymers are macromolecules that form separate distinct domains

958 based on microphase separation of their constituent polymer blocks. Depending on the

959 molecular weights and the relative compositions of the copolymer, different nanodomain

960 structures develop. A variety of three-dimensional morphologies can be assembled.[194]

961 Electroplating can be used in combination with self-assembled polymer templates to fabricate

962 nanolattices from several inorganic materials. For example, three dimensionally periodic

963 double-gyroids were fabricated with block copolymers and coated with nickel using

964 electroplating; after removing the block copolymer, the resulting structure was a periodic

965 double-gyroid nickel replica with strut sizes of 13 nm and a relative density of 38%.[9]

966 Vanadium pentoxide gyroid structures were fabricated using a similar process and with strut

967 sizes of only 10 nm.[195] Room-temperature oxidation of silicon containing triblock copolymers

968 was shown to create silicon oxycarbide inverse double gyroids with strut sizes of ~20 nm.[196]

969　The self-assembly of colloidal crystals using nanoscale particles is another approach for the

970　production of templates for ordered nanoporous structures. Inverse opals made using materials

971　such as silica, nickel and alumina have been reported.[2,197] Typical pore sizes are in the range

972　of a few hundreds of nanometers[2,197,198] and strut thicknesses are on the order of 100 nm[2,197].

973　The technological potential of colloidal self-assembly for large area fabrication has been

974　demonstrated using nickel inverse opals that were fabricated covering 2 cm^2 areas.[197] Inverse

975　opals are open-cell structures, when close-packed colloidal spheres are used as a template.

976　Closed-cell structures can be produced using a colloidal crystal template composed of close

977　packed core–shell spheres that have been infiltrated with a precursor fluid.[199] In a process

978　similar to nanocasting[200], the precursor is converted into the target material and replicates the

979　templated nanomorphology after the chemical removal of the hard template. Colloidal crystals

980　made from carbon and silica and from silica spheres have been identified as the most promising

981　template materials.[200] While colloidal crystals from monodisperse spheres have a limited range

982　of crystal structures, binary mixtures of differently sized colloidal particles were demonstrated

983　to form more complex topologies.[201,202]

984　Three-dimensional assembly of graphene and carbon nanotubes have been predicted by

985　molecular dynamic simulations to possess a number of outstanding physical properties

986　including mechanical, electrical, and chemical.[203–206] Synthesis of nanostructures such as

987　pillared graphene has been shown,[207] but their structural order is limited and they generally do

988　not possess a truly periodic architecture.

989　The application of self-assembly processes to the controlled fabrication of nanolattices is still

990　in its infancy, but their implementation has great potential benefits for upscaling and mass

991　fabrication. The two main advantages of self-assembly methods are their low-cost of synthesis

992　and their rapid processing times. The disadvantages are the limited topological diversity and

993　the emergence of larger-scale defects that typically propagate through the entire material; these

994 both need to be explored in more detail for self-assembly methods to be a truly effective

995 nanolattice fabrication tool.
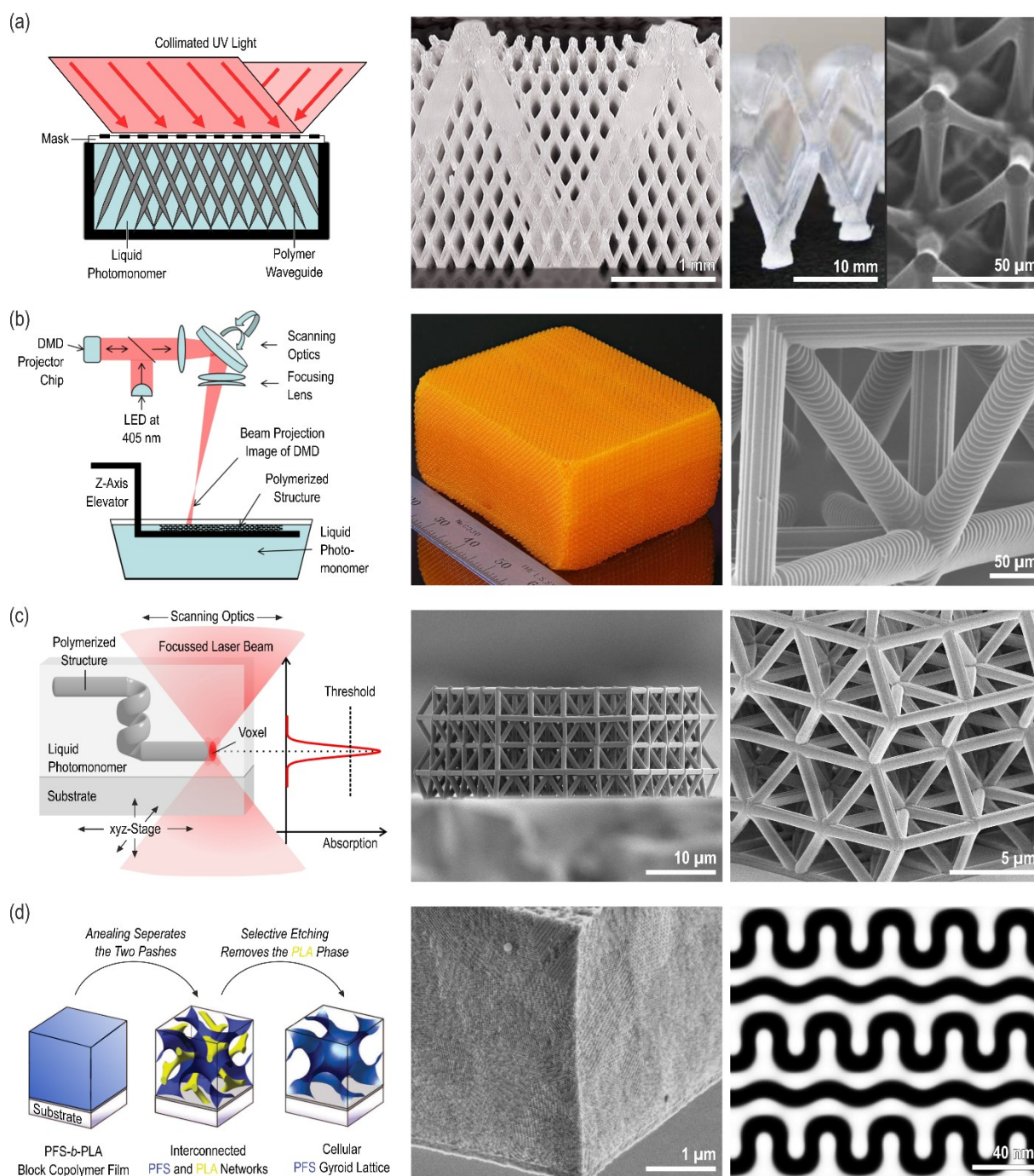
996

997 **Figure 9. Selected processes for fabricating micro- and nanolattices.** (a) By UV-light
998 exposure of a photomonomer through a two-dimensional mask, SPPW creates polymeric
999 microlattices, tens of centimeters in size, within minutes; while topologies are limited to linear
1000 extensions of the mask, feature dimensions may be varied in a broad range, from >25 mm thick
1001 single unit cell structures to lattices with members ~10 µm in diameter, to hierarchical
1002 structures. (b) Large area PµSL creates centimeter-size arbitrary polymeric microstructures
1003 with minimal feature dimensions of 5-300 µm, in a layer-by-layer fashion by polymerizing the
1004 surface layer of a photomonomer bath through a digital mask. (c) DLW processes focus a laser

1005   beam into a photomonomer, creating an ellipsoid shaped polymer feature (voxel) down to
1006   100 nm in size, via multi-photon polymerization. Scanning the laser beam and moving the
1007   sample stage forms arbitrary micro- and nanostructures of typically <1 mm overall size. (d)
1008   Self-assembly i.e. of block copolymers like poly(4-fluorostyrene-block-D,L-lactide) (PFS-b-
1009   PLA), can create a number of topologies such as gyroid lattices, with feature sizes down to
1010   10 nm and overall dimensions of up to centimeters. Adopted from [83,208] and reproduced with
1011   permission, [19] 2014 ,[15] 2011, The American Association for the Advancement of Science,
1012   [209] 2017, Nanoscribe GmbH, [107] 2015, Elsevier, [210] 2009, American Chemical Society.

1013   **3.5. Synthesis of Composite, Ceramic and Metal Structures**

1014   To date, there are no metal- or ceramic-based AM processes with sufficiently high resolution

1015   for the synthesis of nanolattices. The majority of fabrication techniques are polymer-based, and

1016   a number of post-processing techniques exist that are used to overcome this limitation.

1017   *Atomic layer deposition (ALD)* is a highly conformal deposition process that allows for the

1018   coating of complex 3D geometries with angstrom-level thickness control.[211] ALD in its

1019   simplest form is a thermal process that works by depositing a monolayer of a precursor onto a

1020   surface then flowing a reactant over it, resulting in a single atomic layer of a given material.

1021   This cycle can be repeated until a specific material thickness is obtained. More complex forms

1022   of ALD can use multiple precursors and plasma ignition to facilitate less thermodynamically

1023   favorable chemical reactions. ALD is highly advantageous due to its lack of directional

1024   dependence and its ability to diffuse into small spaces, making it ideal for coating polymeric

1025   nanolattices to form core-shell composite structures[2,14] **(Figure 10a)**. Composite structures

1026   can be cut open, e.g. by focused ion beam milling, allowing for the removal of the polymer core

1027   by etching or thermal treatment.[13,198] The major limitation of ALD is its slow rate, which is

1028   normally on the order of nanometers per hour. ALD can be used to create a wide range of

1029   materials, including metals, ceramics, and semiconductors.[212]

1030   *Electroless plating* of metals is a well-established method for coating a broad range of shapes

1031   and materials.[213] Preferred are metals with a reduction potential greater than that of water, so

1032   that they can be deposited in aqueous solutions. Ionic liquid based processes have been

1033 developed for important metals with a low reduction potential such as aluminum. Electroless

1034 deposition is a favorable method for the coating of lattice materials with metals due to the

1035 conformal, non-line-of-sight deposition characteristics[15]. Electroless plating processes rely on

1036 an autocatalytic reaction to reduce the metal ions in solution; it therefore enables the uniform

1037 deposition into pores as long as mass transport is not limited. Hollow-beam metal lattices can

1038 be fabricated in a process analogous to that illustrated in Figure 10a.

1039 *Electroplating* into negative templates enables the fabrication of solid-beam metallic lattices

1040 (Figure 10b).[9,89] This process involves first spinning a positive tone photoresist, i.e. a

1041 photoresist that is designed to be removed after exposure to UV light, onto a conductive

1042 substrate. Transparent conductive substrates can be made using thin films of indium tin oxide

1043 (ITO) or gold, which remain sufficiently transparent when sputtered at thicknesses of <50 nm.

1044 Using AM techniques, a structure can then be written into the photoresist, with the requirement

1045 that it must span from the top of the spun photoresist to the conductive substrate in order to

1046 ensure a conductive path. After the exposed resist has been developed, the pores can be

1047 infiltrated with an electroplateable material. Electroplating is a commonly utilized industrial

1048 process, and has been shown to offer a high degree of nanostructural material control.[214] In

1049 contrast to electroless plating, electroplating uses an applied voltage from an external source to

1050 deposit a material from solution. Deposition rates are proportional to the current density in the

1051 part, which also depends on the electric field applied by the anodes. The application of a

1052 constant voltage can result in a moderate directional dependence and deposition that is limited

1053 by line of sight. With advanced electroplating techniques such as voltage pulsing and conformal

1054 anodes, metal can readily be deposited into complex, three-dimensional nanoscale pores.

1055 Multiple metals can be electroplated in parallel, but complexity increases exponentially with

1056 every additional metal; electroplating is therefore not well suited for the creation of

1057 multicomponent alloys. Care must be taken to ensure that the electroplating solution does not

1058 react with and erode the photoresist. After electroplating, the undeveloped photoresist can be

1059 removed using a developer, leaving behind a solid lattice.

1060 Using *pyrolysis*, glassy carbon-based structures (Figure 10c) can be made from thermosetting

1061 polymers, such as UV-cured resins, that are thermally decomposed in vacuum or inert

1062 atmosphere at temperatures in the range of 1000-3000°C.[215] This process is accompanied by

1063 shrinkages of up to 90%.[216] Glassy carbon is an amorphous carbon allotrope that primarily

1064 consists of non-graphitic sp^2-bonded carbon.[99,216] The fabrication of nanolattices using

1065 pyrolysis offers two unique benefits. (I) Polymer templates are directly transformed to robust

1066 ceramic structures, avoiding procedures like coating, milling and etching. Glassy carbon

1067 exhibits excellent chemical and thermal stability as well as biocompatibility and can achieve

1068 semiconductor-type electrical properties.[216] Its Young's modulus is about 10 times higher than

1069 that of cross-linked epoxy resins[217], and strengths in nanolattices on the order of 3 GPa have

1070 been observed. Its low density[99,215] of 1.3-1.5 g/cm³ is attributed to a fullerene-related closed-

1071 cell porosity[218]. Silicon-based pre-ceramic resins can be used to fabricate pre-ceramic polymer

1072 lattices via UV-curing, which then can be converted to ceramics such as silicon-oxycarbide[84].

1073 (II) With appropriate designs, highly uniform shrinkage can be exploited to fabricate

1074 considerably smaller structures than what is achievable with the applied fabrication method

1075 alone. A five-fold reduction in size was demonstrated with direct-laser written octet lattices

1076 (Figure 10c).[1]

1077 AM with *particle-loaded polymers* allows for the fabrication of macro- and microlattices from

1078 a variety of materials. The most common of these processes use inorganic particles like oxides

1079 embedded in a thermoset polymer that become sintered after the polymer is burned off[19]. Metal

1080 particles can also be used, and good results have been achieved with copper and silver.[219]

1081 Carbon fiber reinforced polymer composites[220] as well as foam based ceramic lattices[221] have

1082 also been processed. The major drawbacks of this method are that the final material is likely to

1083 possess a high flaw population, and the reduced resolution and feature quality. Both of these

1084 makes particle-loaded AM techniques difficult to use for the fabrication of nanolattices.

1085 Lithographically defined microstructures of graphene oxide flakes with feature sizes on the

1086 order of 1 μm[222] as well as high-quality, transparent fused silica microstructures[223] have been

1087 shown, though.
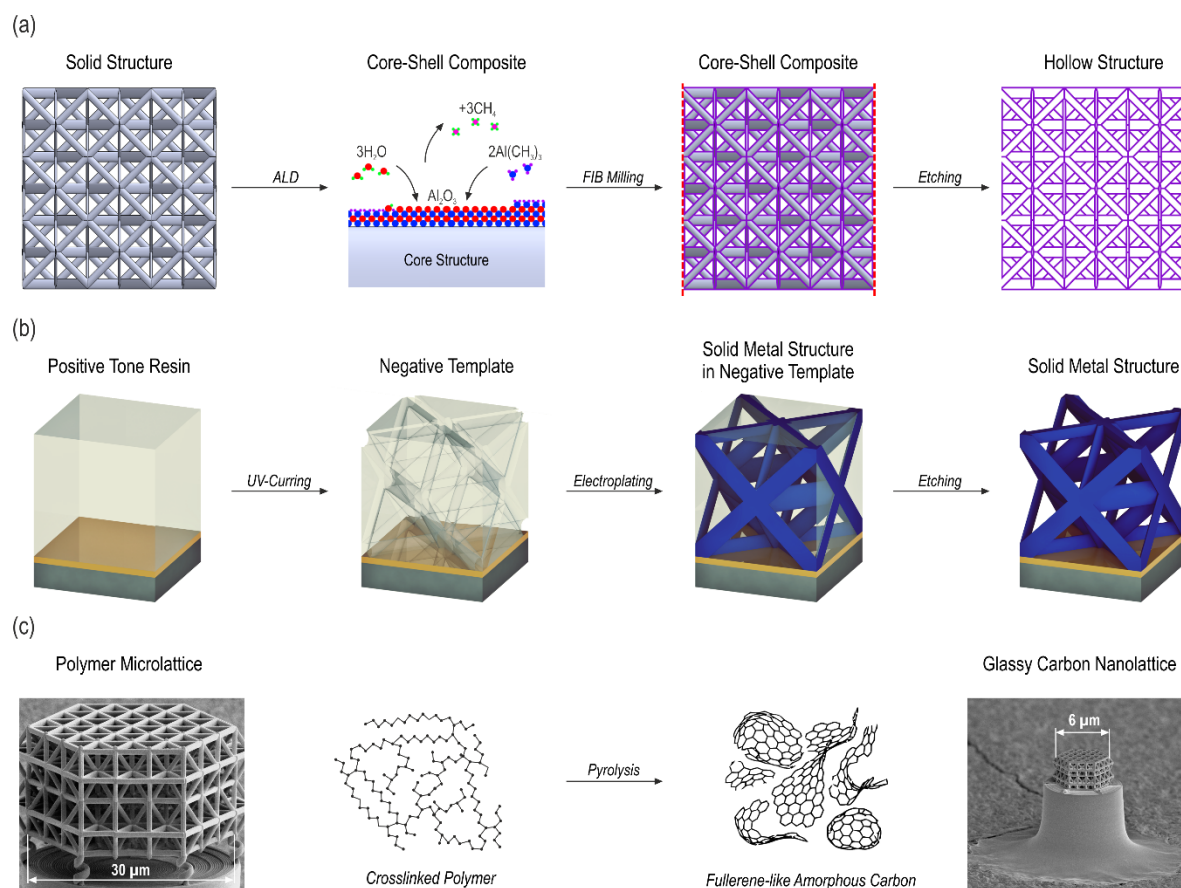
1088

1089 **Figure 10. Post-processing routes for synthesizing ceramic, metallic and composite**
1090 **nanolattices based on polymer templates.** (a) Hollow-beam ceramic lattices are fabricated by
1091 ALD, focused ion beam (FIB) milling and etching; analogously, metal lattices can be made via
1092 electroless plating. (b) Electroplating into a negative template creates solid-beam metal lattices.
1093 (c) Accompanied by conformal shrinkage of up to 90%, pyrolysis of polymer lattices yields
1094 carbon-based ceramic lattices. Adopted from [1] and reproduced with permission, [13] 2014, The
1095 American Association for the Advancement of Science, [89] 2015, Elsevier.

1096 **4. Hierarchical Architecture & Scale-Up**

1097 The exceptional properties of nanolattices can only truly have an impact as engineering

1098 materials if they are scaled-up to sizes that are relevant for technological applications. Scaling-

1099 up the dimensions of a structure while keeping its smallest feature sizes at the nanoscale is

1100   inherently difficult, and current fabrication methods dictate a tradeoff between build volume,

1101   production rate and minimum feature size. The most straightforward workaround to overcome

1102   this problem is to combine large-scale, high-throughput processes with thin film deposition

1103   techniques to produce hollow structures, but any length scale gaps in the architecture will

1104   inevitably lead to shell buckling instabilities due to high ratios of diameter-to-wall-thickness[15].

1105   Hierarchical architecture provides a means of expanding build volumes without sacrificing

1106   accuracy, resolution or structural integrity. The production rates of many AM processes scale

1107   proportionally to the relative density of the structure being manufactured. The effective relative

1108   density ($\bar{\rho}_{eff}$) of a hierarchical structure compounds with increasing hierarchical order, and for

1109   an architecture of order N is given approximately by

1110 $$\bar{\rho}_{eff} = \prod_1^N \bar{\rho}_i, \tag{8}$$

1111   where $\bar{\rho}_i$ is the relative density of the ith level of hierarchy. When the order of hierarchy is

1112   increased, the compounding relative densities decrease the effective relative density without

1113   increasing the slenderness of individual structural elements, thereby maintaining structural

1114   stability.

1115   A scaled-up manufacturing of microlattices with nanoscale features from hundreds of

1116   micrometers to several centimeters has been demonstrated using large area PμSL.[83] **Figure 11**

1117   shows a breakdown of the feature sizes in these materials, the length scale of each order of

1118   structural hierarchy decreases by a factor of ~10 from one level to the next. The microlattice

1119   consists of a network of octet unit cells (Figure 11c) comprised of strut members that are

1120   ~200 μm in diameter, each of which consist of a network of self-similar smaller-scale unit cells

1121   (Figure 11h). The first-order unit cells are made from hollow tube nickel–based struts (Figure

1122   11i) with diameters on the order of 10 μm and wall thicknesses ranging from 50 nm to 700 nm

1123   (Figure 11j). Similar orders of structural hierarchy has been shown in nanolattices made from

1124   both core-shell polymer-alumina and hollow alumina with first-order strut diameters below

1125   1 μm and shell thicknesses of 20 nm, and an overall structure size on the order of hundreds of

1126   micrometers.[82]
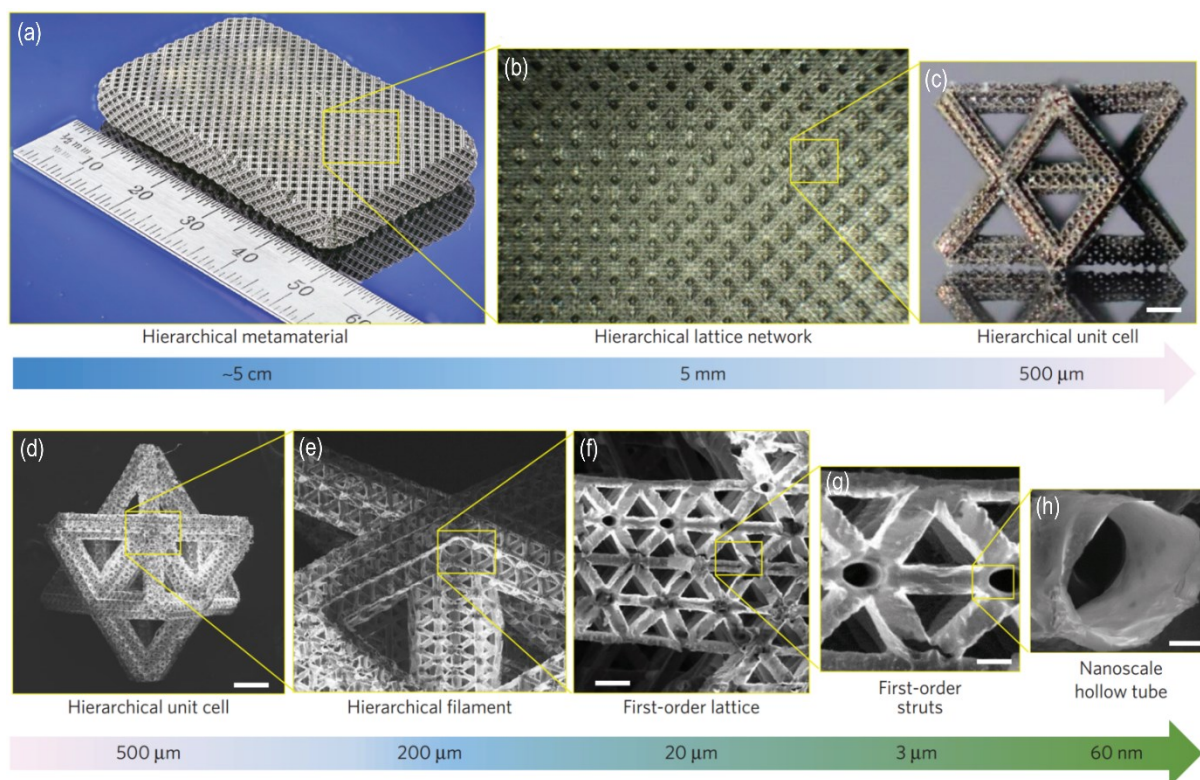
1127

Figure 11. Centimeter-size hierarchical hollow-beam nickel microlattice material fabricated using large area projection micro-stereolithography. (a-c) Optical microscope images of bulk hierarchical lattice material with a network of hierarchical octet unit cells. (d)-(h) Scanning electron micrographs showing the breakdown of structural hierarchy down to hollow-beam walls tens of nanometers in thickness. The scale bar is 80 μm in (c) and 3 μm in (h). Adopted from [83].

1134   Hierarchical architectures offer a range of unique mechanical properties that are widely taken

1135   advantage of in the natural world (Figure 3).[68,69] Diatom frustules, Euplectella glass sponges,

1136   and bone have exceptional resilience to mechanical loading. Soft tissues such as skin and

1137   structures like bird's nests are highly compliant and able to undergo large deformations without

1138   failure. A number of man-made structures have been created that have hierarchical architectures,

1139   the most common of which are construction cranes and building scaffolding, and the most

1140   notable example being the Eiffel tower[224]. One key advantage of both natural and engineered

1141   hierarchical structures is their increased resistance to buckling. Recalling the Euler buckling

1142 criterion from Section 2.1.2, the buckling strength of a beam scales with its length as $1/l^2$, and

1143 the resulting strength of a buckling-dominated lattice scales with relative density as $\sigma \propto \bar{\rho}^2$. In

1144 a hierarchical structure, the relative densities at each order of hierarchy are multiplied according

1145 to Equation 8, meaning beam length and relative density are decoupled. The length of the beams

1146 can therefore be much shorter for a given $\bar{\rho}$ compared to a single-order structure, resulting in

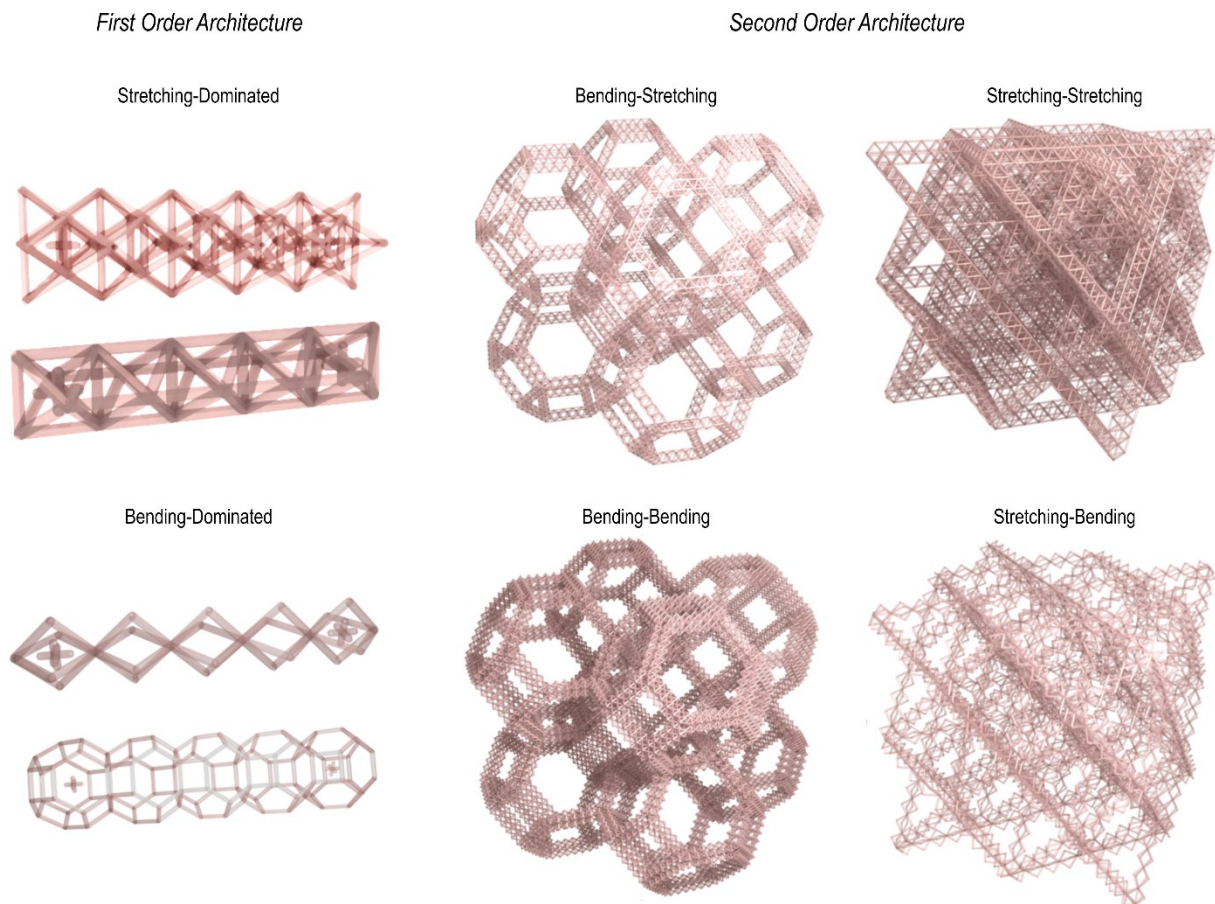1147 an increase in the buckling resistance.

1148 There are four different types of hierarchical lattice architectures that can be created using

1149 stretching- and bending-dominated constituent lattices **(Figure 12)**.[49] Combinations of self-

1150 similar architectures at adjacent hierarchical levels result in fractal-like lattices that are either

1151 stretching-stretching or bending-bending. Combining dissimilar architectures at neighboring

1152 hierarchies results in hybrid lattices that are either stretching-bending or bending-stretching. In

1153 all four cases, the effective strength (σ_{eff}) of a hierarchical structure of order N can be

1154 approximated by the first order scaling law

1155 $\sigma_{eff} = C_{eff} \prod_1^N \bar{\rho}_i^{a_i} \sigma_s$ (9)

1156 where σ_s is the strength of the constituent solid material, C_{eff} is an effective geometric

1157 parameter, and a_i is the scaling exponent of each order. Similarly, the effective stiffness (E_{eff})

1158 can be estimated by,

1159 $E_{eff} = F_{eff} \prod_1^N \bar{\rho}_i^{g_i} E_s$ (10)

1160 where E_s is the Young's modulus of the constituent solid material and F_{eff} is an effective

1161 geometric parameter.

First Order Architecture | Second Order Architecture

Stretching-Dominated | Bending-Stretching | Stretching-Stretching

Bending-Dominated | Bending-Bending | Stretching-Bending

1162

Figure 12. Different types of hierarchical lattice architectures. Mechanical behavior can be tailored for high strength and stiffness (stretching-stretching), high compliance (bending-bending) or the intermediate cases of both (bending-stretching, stretching-bending). Adopted from [83].

Fractal-like stretching-dominated hierarchy can lead to superior strength at low density due to an increased buckling stability, potentially enabling access to ultra-low density material property spaces that are inaccessible to first order lattices. Tunable failure behavior and increased energy absorption has been demonstrated with lattices[82,83], honeycombs and sandwich panels[225–227], and corrugated truss[228] and space frame structures[229]. Fractal-like stretching-dominated micro-[83] and nanolattices[82] have exhibited near-linear scaling of strength and stiffness down to $\bar{\rho} \approx 0.01\%$ (Figure 4 and Figure 6), while corresponding first order lattices[13,19] have scaling exponents as high as 2.7 below $\bar{\rho} \approx 0.1\%$. The geometric parameters of the hierarchical orders have a multiplying effect due to the underutilization of non-axially oriented lattice elements; this can lead to a reduction in the effective properties. For

1177 example, the effective geometric parameter of an octet lattice decreases from 1/3 to 1/9 as a

1178 structure goes from first- to second-order, which results in a decrease of σ_{eff} by a factor of

1179 three. This same mechanism has the effect of increasing the damage tolerance. After axially

1180 oriented lattice elements undergo failure, non-axially oriented elements are able to remain intact

1181 and distribute strain through bending or local elastic buckling, thereby accommodating large

1182 global deformation without failure.[82] Recoverabilities of up to 98% of the original structure

1183 height after compression to ≥50% have been reported.[82] Corresponding to Section 2.3, the

1184 introduction of hierarchy increases the tailorability of failure modes and post-failure behavior.

1185 Based on classical lattice theory, stiffness cannot be increased by the addition of hierarchy to

1186 the architecture, but it has been postulated that the introduction of hierarchy can reduce local

1187 bending effects in certain structures, leading to an increase in the effective stiffness.[82]

1188 Fractal-like bending-dominated hierarchies can be used to create highly compliant structures.

1189 A second-order lattice with $g_1 = g_2 = 2$ has an effective scaling exponent between stiffness

1190 and relative density of four. This can potentially allow for large, super-elastic deformations

1191 even with brittle base materials. Combining bending-dominated architectures may not always

1192 result in an increased compliance. In contrast to stretching-dominated hierarchies, the geometric

1193 parameters of each bending-dominated hierarchical order adds up, leading to an increased

1194 effective stiffness.[226,230] This can be understood as a gain in flexural rigidity for a given relative

1195 density that occurs when replacing slender lattice elements with a bending-dominated network

1196 of smaller-scale, short and squat elements. A similar behavior applies for the effective

1197 strength.[226]

1198 Combining stretching- and bending dominated architectures yields mixed behavior. A cuboid-

1199 octet microlattice optimized for tensile loading has been constructed by tessellating a first-order

1200 stretching-dominated topology with a second-order bending-dominated one.[83] The

1201 microlattice was comprised of brittle 60 nm nickel-based thin films but still demonstrated

1202 reversible elastic stretching up to 20% strain; this was achieved while simultaneously attaining

1203 specific tensile strengths substantially higher than commercial foams and comparable to those

1204 of first order core-shell polymer-ceramic lattices[87] synthesized using DLW.[83] While the

1205 stiffness of these materials was governed by compliant hinges in the bending-dominated second

1206 order of hierarchy, their high strength has been attributed to mechanical size-effects in the

1207 hollow-beam walls of the first-order architecture. Ceramic honeycomb structures fabricated

1208 using direct foam writing with a bending-dominated first order topology and a stretching-

1209 dominated second order architecture were shown to possess highly tailorable stiffness.[221] The

1210 effective geometric parameter of bending-stretching architectures increases with the number of

1211 hierarchical orders in a similar manner to fractal-like bending architectures. The reverse is true

1212 for stretching-bending type architectures; as the elements of the stretching-dominated lattice

1213 are replaced by bending-dominated ones, they deform by bending instead of stretching,

1214 resulting in reduced stiffness compared to the first-order stretching-dominated architecture.

1215 **5. Conclusion & Outlook**

1216 The introduction of lattice architecture at the micro- and nanoscale has set new boundaries on

1217 the accessible regions of many material property spaces. Photonic and phononic metamaterials

1218 with periodicity comparable to the wavelength of optical or acoustic waves were the first drivers

1219 towards miniaturization. The high strengths of nanolattices for the first time strikingly

1220 demonstrated the ability to exploit size effects in mechanical metamaterials. Simultaneously

1221 nanolattice architecture can be designed to enable unique scale-independent properties such as

1222 tailorable stiffness, deformability, thermal expansion, as well as auxetic behavior and

1223 pentamode meta-fluidity. It is the confluence of nanomaterials and architecture that engenders

1224 the huge diversity of properties of nanolattices, although not all properties explicitly benefit

1225 from miniaturization.

The extensive work on nanolattices in the recent years has laid the foundation for this emerging field. Data is still very limited and key physical principles, including some of those described here, are the subject of some uncertainty. More in depth characterization and modeling are still required to draw a comprehensive picture. Due to experimental limitations, investigations into the mechanical behavior of nanolattices has mostly been limited to compression tests, and proper assessment of their tensile, shear, and fracture properties needs to be done. Besides strength, many more mechanical, or thermal and electrical properties exhibit size-dependent behavior. Incorporation of these effects in nanolattices would inevitably lead to major advances in the colonization of new material property space, and bears the potential for creating new materials with superior multifunctionality. Approaches for creating metamaterials may vary widely across disciplines, but it is remarkable how similar optimal architectures and scales often are. Moving forward, nanolattices should not be thought of as photonic, phononic, auxetic, or light-weight metamaterials, but instead as a single class of multifunctional materials. As nature shows, the introduction of hierarchy is crucial to achieve both multifunctionality and optimized individual properties like mechanical robustness. Initial efforts for the introduction of structural hierarchy into nanolattices have been promising, and eventual designs may be able to fully mimic the material hierarchy of biological materials, leading to a new generation of multifunctional nanolattice materials.

Size-effects in materials have been investigated for decades, and nanolattices provide a promising avenue for the preservation of superior size-affected properties in large-scale materials applications. A major future challenge will be to substantially push the current limits of scalability to create nanolattices with sizes that are relevant for technical applications. Some potential methods to increase production while maintaining nanoscale features are parallelization by diffractive beam splitting of laser techniques such as DLW, multi-step self-assembly, and hybrid fabrication methods that combine AM with extrusion or injection molding.

1251 These fabrication methods have a number of technological challenges associated with their
1252 implementation, the most critical of which being that they avoid introducing macroscopic flaws
1253 that counteract the beneficial properties gained from using nanomaterials. Another challenge is
1254 extending the narrow bandwidth of materials available for manufacturing of nanolattices.

1255 The first market for nanolattices may be small-scale, small-lot components for biomedical,
1256 electrochemical, microfluidic and aerospace applications, which require highly customizable
1257 and extreme combinations of properties. Should scalability become a reality, nanolattices will
1258 find application in a variety of lightweight structural components. Over the past few years,
1259 nanolattices have certainly caught the attention of scientists and engineers alike. The scientific
1260 and technological development over the next few decades will be critical for moving this
1261 exciting new class of materials from the lab bench to our everyday life.

1262
1263
1264

Acknowledgements

1269

1273

1274

References

[1] J. Bauer, A. Schroer, R. Schwaiger, O. Kraft, *Nat. Mater.* **2016**, *15*, 438.

[2] J. J. do Rosário, E. T. Lilleodden, M. Waleczek, R. Kubrin, A. Y. Petrov, P. N. Dyachenko, J. E. C. Sabisch, K. Nielsch, N. Huber, M. Eich, G. A. Schneider, *Adv. Eng. Mater.* **2015**, DOI 10.1002/adem.201500118.

[3] J. J. do Rosário, J. B. Berger, E. T. Lilleodden, R. M. McMeeking, G. A. Schneider, *Extrem. Mech. Lett.* **2016**, *in press*, DOI 10.1016/j.eml.2016.07.006.

[4] A. J. Jacobsen, W. B. Carter, S. Nutt, *Adv. Mater.* **2007**, *19*, 3892.

[5] X. Zheng, J. Deotte, M. P. Alonso, G. R. Farquar, T. H. Weisgraber, S. Gemberling, H. Lee, N. Fang, C. M. Spadaccini, *Rev. Sci. Instrum.* **2012**, *83*, 125001.

[6] S. Maruo, O. Nakamura, S. Kawata, *Opt. Lett.* **1997**, *22*, 132.

[7] A. Selimis, V. Mironov, M. Farsari, *Microelectron. Eng.* **2014**, *132*, 83.

[8] X. Li, H. Gao, *Nat. Mater.* **2016**, *15*, 373.

[9] S. N. Khaderi, M. R. J. Scherer, C. E. Hall, U. Steiner, U. Ramamurty, N. A. Fleck, V. S. Deshpande, *Extrem. Mech. Lett.* **2016**, DOI 10.1016/j.eml.2016.08.006.

[10] N. Kröger, *Curr. Opin. Chem. Biol.* **2007**, *11*, 662.

[11] J. Parkinson, R. Gordon, *Trends Biotechnol.* **1999**, *17*, 190.

[12] D. Losic, J. G. Mitchell, N. H. Voelcker, *Adv. Mater.* **2009**, *21*, 2947.

[13] L. R. Meza, S. Das, J. R. Greer, *Science* **2014**, *345*, 1322.

[14] J. Bauer, S. Hengsbach, I. Tesari, R. Schwaiger, O. Kraft, *Proc Natl Acad Sci USA* **2014**, *111*, 2453.

[15] T. A. Schaedler, A. J. Jacobsen, A. Torrents, A. E. Sorensen, J. Lian, J. R. Greer, L. Valdevit, W. B. Carter, *Science* **2011**, *334*, 962.

[16] L. Valdevit, S. W. Godfrey, T. a. Schaedler, A. J. Jacobsen, W. B. Carter, *J. Mater. Res.* **2013**, *28*, 2461.

[17] A. Torrents, T. A. Schaedler, A. J. Jacobsen, W. B. Carter, L. Valdevit, *Acta Mater.* **2012**, *60*, 3511.

[18] K. J. Maloney, C. S. Roper, A. J. Jacobsen, W. B. Carter, L. Valdevit, T. A. Schaedler, *APL Mater.* **2013**, *1*, DOI 10.1063/1.4818168.

[19] X. Zheng, H. Lee, T. H. Weisgraber, M. Shusteff, J. DeOtte, E. B. Duoss, J. D. Kuntz, M. M. Biener, Q. Ge, J. A. Jackson, S. O. Kucheyev, N. X. Fang, C. M. Spadaccini, *Science* **2014**, *344*, 1373.

[20] T. Bückmann, N. Stenger, M. Kadic, J. Kaschke, A. Frölich, T. Kennerknecht, C. Eberl, M. Thiel, M. Wegener, *Adv. Mater.* **2012**, *24*, 2710.

[21] M. Kadic, T. Bückmann, N. Stenger, M. Thiel, M. Wegener, *Appl. Phys. Lett.* **2012**, *100*, DOI 10.1063/1.4709436.

[22] T. Ergin, N. Stenger, P. Brenner, J. B. Pendry, M. Wegener, *Science* **2010**, *328*, 337.

[23] J. Fischer, T. Ergin, M. Wegener, *Opt. Lett.* **2011**, *36*, 2059.

[24] J. K. Gansel, M. Thiel, M. S. Rill, M. Decker, K. Bade, V. Saile, G. Von Freymann, S. Linden, M. Wegener, *Science* **2009**, *325*, 1513.

[25] A. G. Bell, *Natl. Geogr. Mag.* **1903**, *14*, 219.

[26] J. Baldwin, *BuckyWorks : Buckminster Fullers Ideas for Today*, Wiley, New York, **1996**.

[27] E. Arzt, *Acta Mater.* **1998**, *46*, 5611.

[28] G. AA, *Phil Trans R Soc L. A* **1921**, *221*, 163.

[29] H. Gao, B. Ji, I. L. Jaeger, E. Arzt, P. Fratzl, *Proc Natl Acad Sci USA* **2003**, *100*, 5597.

[30] O. Kraft, P. A. Gruber, R. Mönig, D. Weygand, *Annu. Rev. Mater. Res.* **2010**, *40*, 293.

[31] J. R. Greer, J. T. M. De Hosson, *Prog. Mater. Sci.* **2011**, *56*, 654.

[32] L. H. Liang, B. Li, *Phys. Rev. B - Condens. Matter Mater. Phys.* **2006**, *73*, 1.

1324 [33] A. a Balandin, S. Ghosh, W. Bao, I. Calizo, D. Teweldebrhan, F. Miao, C. N. Lau,
1325 *Nano Lett.* **2008**, *8*, 902.
1326 [34] D. Josell, S. H. Brongersma, Z. Tőkei, *Annu. Rev. Mater. Res.* **2009**, *39*, 231.
1327 [35] M. S. Dresselhaus, G. Chen, M. Y. Tang, R. Yang, H. Lee, D. Wang, Z. Ren, J. P.
1328 Fleurial, P. Gogna, *Adv. Mater.* **2007**, *19*, 1043.
1329 [36] N. Hansen, *Scr. Mater.* **2004**, *51*, 801.
1330 [37] T. Zhu, J. Li, S. Ogata, S. Yip, *MRS Bull.* **2009**, *34*, 167.
1331 [38] G. Stan, S. Krylyuk, A. V. Davydov, I. Levin, R. F. Cook, *Nano Lett.* **2012**, *12*, 2599.
1332 [39] X. Han, K. Zheng, Y. Zhang, X. Zhang, Z. Zhang, Z. L. Wang, *Adv. Mater.* **2007**, *19*,
1333 2112.
1334 [40] D.-M. Tang, C.-L. Ren, M.-S. Wang, X. Wei, N. Kawamoto, C. Liu, Y. Bando, M.
1335 Mitome, N. Fukata, D. Golberg, **2012**.
1336 [41] D. Z. Chen, D. Jang, K. M. Guan, Q. An, W. A. Goddard, J. R. Greer, *Nano Lett.* **2013**,
1337 *13*, 4462.
1338 [42] D. Jang, J. R. Greer, *Nat. Mater.* **2010**, *9*, 215.
1339 [43] M. P. Manoharan, H. Lee, R. Rajagopalan, H. C. Foley, M. a. Haque, *Nanoscale Res.*
1340 *Lett.* **2010**, *5*, 14.
1341 [44] C. Lee, X. Wei, J. W. Kysar, J. Hone, *Science* **2008**, *321*, 385.
1342 [45] B. I. Yakobson, P. Avouris, in *Carbon Nanotub. Synth. Struct. Prop. Appl.* (Eds.: M.S.
1343 Dresselhaus, G. Dresselhaus, P. Avouris), Springer, Berlin, **2001**, pp. 287–327.
1344 [46] K. Kawamura, G. Jenkins, *J. Mater. Sci.* **1970**, *5*, 262.
1345 [47] A. Mathur, J. Erlebacher, *Appl. Phys. Lett.* **2007**, *90*, 2005.
1346 [48] C. Ensslen, C. Brandl, G. Richter, R. Schwaiger, O. Kraft, *Acta Mater.* **2016**, *108*, 317.
1347 [49] N. A. Fleck, V. S. Deshpande, M. F. Ashby, *Proc. R. Soc. A Math. Phys. Eng. Sci.*
1348 **2010**, *466*, 2495.
1349 [50] V. S. Deshpande, M. F. Ashby, N. A. Fleck, *Acta Mater.* **2001**, *49*, 1035.
1350 [51] L. J. Gibson, M. F. Ashby, *Cellular Solids: Structure and Properties*, Cambridge Univ.
1351 Pr., Cambridge, UK, **2001**.
1352 [52] V. S. Deshpande, N. A. Fleck, M. F. Ashby, *J. Mech. Phys. Solids* **2001**, *49*, 1747.
1353 [53] L. Dong, V. S. Deshpande, H. N. G. Wadley, *Int. J. Solids Struct.* **2015**, *60*, 107.
1354 [54] T. George, V. S. Deshpande, H. N. G. Wadley, *Compos. PART A* **2013**, *47*, 31.
1355 [55] L. Salari-Sharif, T. A. Schaedler, L. Valdevit, *J. Mater. Res.* **2014**, *29*, 1755.
1356 [56] C. A. Steeves, S. L. dos Santos e Lucato, M. He, E. Antinucci, J. W. Hutchinson, A. G.
1357 Evans, *J. Mech. Phys. Solids* **2007**, *55*, 1803.
1358 [57] J. T. B. Overvelde, T. A. de Jong, Y. Shevchenko, S. A. Becerra, G. M. Whitesides, J.
1359 C. Weaver, C. Hoberman, K. Bertoldi, *Nat. Commun.* **2016**, *7*, 10929.
1360 [58] X. Hou, V. V Silberschmidt, in *Mech. Adv. Mater. Anal. Prop. Perform.* (Eds.: V. V
1361 Silberschmidt, V.P. Matveenko), Springer International Publishing, Cham, **2015**, pp.
1362 155–179.
1363 [59] R. Schittny, T. Bückmann, M. Kadic, M. Wegener, *Appl. Phys. Lett.* **2013**, *103*, 1.
1364 [60] J. Christensen, M. Kadic, M. Wegener, O. Kraft, *MRS Commun.* **2015**.
1365 [61] A. A. Zadpoor, *Mater. Horiz.* **2016**, *3*, 371.
1366 [62] M. Maldovan, E. L. Thomas, *Periodic Materials and Interference Lithography: For*
1367 *Photonics, Phononics and Mechanics*, Wiley, **2009**.
1368 [63] C. M. Soukoulis, M. Wegener, *Nat. Photonics* **2011**, *5*, 523.
1369 [64] G. von Freymann, A. Ledermann, M. Thiel, I. Staude, S. Essig, K. Busch, M. Wegener,
1370 *Adv. Funct. Mater.* **2010**, *20*, 1038.
1371 [65] M. Maldovan, *Nature* **2013**, *503*, 209.
1372 [66] M. I. Hussein, M. J. Leamy, M. Ruzzene, *Appl. Mech. Rev.* **2014**, *66*, 40802.
1373 [67] T. Bückmann, R. Schittny, M. Thiel, M. Kadic, G. W. Milton, M. Wegener, *New J.*
1374 *Phys.* **2014**, *16*, 33032.

1375 [68] P. Fratzl, R. Weinkamer, *Prog. Mater. Sci.* **2007**, *52*, 1263.

1376 [69] M. A. Meyers, P. Chen, A. Y. Lin, Y. Seki, **2008**, *53*, 1.

1377 [70] F. E. Round, R. M. Crawford, D. G. Mann, *Diatoms: Biology and Morphology of the*
1378   *Genera*, Cambridge University Press, Cambridge, UK, **1990**.

1379 [71] C. E. Hamm, R. Merkel, O. Springer, P. Jurkojc, C. Maier, K. Prechtel, V. Smetacek,
1380   *Nature* **2003**, *421*, 841.

1381 [72] S. Weiner, H. D. Wagner, *Annu. Rev. Mater. Sci.* **1998**, *28*, 271.

1382 [73] J. Aizenberg, J. C. Weaver, M. S. Thanawala, V. C. Sundar, D. E. Morse, P. Fratzl,
1383   *Science (80-.).* **2005**, *309*, 275.

1384 [74] J. Wolff, *The Law of Bone Remodeling*, Springer, Berlin, **1986**.

1385 [75] J. Currey, *Bones: Structure and Mechanics*, Princeton Univ Press, Princeton, **2002**.

1386 [76] A. G. M. Michell, *Philos. Mag. Ser. 6* **1904**, *8*, 589.

1387 [77] C. Mattheck, *Design in Nature : Learning from Trees*, Springer, Berlin, **1998**.

1388 [78] E. D. Yilmaz, S. Bechtle, H. Özcoban, A. Schreyer, G. a. Schneider, *Scr. Mater.* **2013**,
1389   *68*, 404.

1390 [79] M. A. Meyers, A. Y.-M. Lin, P.-Y. Chen, J. Muyco, *J. Mech. Behav. Biomed. Mater.*
1391   **2008**, *1*, 76.

1392 [80] A. Jantschke, C. Fischer, R. Hensel, H.-G. Braun, E. Brunner, *Nanoscale* **2014**, *6*,
1393   11637.

1394 [81] C. Mattheck, *Die Körpersprache Der Bauteile: Enzyklopädie Der Formfindung Nach*
1395   *Der Natur*, Karlsruhe Institute Of Technology, Karlsruhe, **2017**.

1396 [82] L. R. Meza, A. J. Zelhofer, N. Clarke, A. J. Mateos, D. M. Kochmann, J. R. Greer,
1397   *Proc. Natl. Acad. Sci. U. S. A.* **2015**, *112*, 11502.

1398 [83] X. Zheng, W. Smith, J. Jackson, B. Moran, H. Cui, D. Chen, J. Ye, N. Fang, N.
1399   Rodriguez, T. Weisgraber, C. M. Spadaccini, *Nat. Mater.* **2016**, DOI
1400   10.1038/nmat4694.

1401 [84] Z. C. Eckel, C. Zhou, J. H. Martin, A. J. Jacobsen, W. B. Carter, T. A. Schaedler,
1402   *Science (80-.).* **2016**, *351*, 58.

1403 [85] A. J. Jacobsen, S. Mahoney, W. B. Carter, S. Nutt, *Carbon N. Y.* **2011**, *49*, 1025.

1404 [86] S. J. Shin, S. O. Kucheyev, M. a. Worsley, A. V. Hamza, *Carbon N. Y.* **2012**, *50*, 5340.

1405 [87] J. Bauer, A. Schroer, R. Schwaiger, O. Kraft, *Adv. Eng. Mater.* **2016**, *18*, 1537.

1406 [88] M. Mieszala, M. Hasegawa, G. Guillonneau, J. Bauer, R. Raghavan, C. Frantz, O.
1407   Kraft, S. Mischler, J. Michler, L. Philippe, *Small* **2017**, *13*, 1602514.

1408 [89] X. W. Gu, J. R. Greer, *Extrem. Mech. Lett.* **2015**, *2*, 7.

1409 [90] L. C. Montemayor, J. R. Greer, *J. Appl. Mech.* **2015**, *82*, 1.

1410 [91] I. C. Cheng, A. M. Hodge, *Scr. Mater.* **2013**, *69*, 295.

1411 [92] J. R. Hayes, A. M. Hodge, J. Biener, A. V Hamza, K. Sieradzki, *J. Mater. Res.* **2006**,
1412   *21*, 2611.

1413 [93] C. A. Volkert, E. T. Lilleodden, D. Kramer, J. Weissmüller, *Appl. Phys. Lett.* **2006**, *89*,
1414   87.

1415 [94] A. M. Hodge, J. Biener, J. R. Hayes, P. M. Bythrow, C. A. Volkert, A. V. Hamza, *Acta*
1416   *Mater.* **2007**, *55*, 1343.

1417 [95] J. Biener, A. M. Hodge, A. V. Hamza, L. M. Hsiung, J. H. Satcher, *J. Appl. Phys.* **2005**,
1418   *97*, 1.

1419 [96] S. O. Kucheyev, M. Stadermann, S. J. Shin, J. H. Satcher, S. A. Gammon, S. A. Letts,
1420   T. Van Buuren, A. V. Hamza, *Adv. Mater.* **2012**, *24*, 776.

1421 [97] S. a Steiner, T. F. Baumann, J. Kong, J. H. Satcher, M. S. Dresselhaus, *Langmuir* **2007**,
1422   *23*, 5161.

1423 [98] E. Krämer, S. Förster, C. Göltner, M. Antonietti, *Langmuir* **1998**, *14*, 2027.

1424 [99] F. C. Cowlard, J. C. Lewis, *J. Mater. Sci.* **1967**, *2*, 507.

1425 [100] M. Berdova, T. Ylitalo, I. Kassamakov, J. Heino, P. T. Törmä, L. Kilpi, H. Ronkainen,

J. Koskinen, E. Hæggström, S. Franssila, *Acta Mater.* **2014**, *66*, 370.

[101] J. Lian, D. Jang, L. Valdevit, T. A. Schaedler, A. J. Jacobsen, W. B. Carter, J. R. Greer, *Nano Lett.* **2011**, *11*, 4118.

[102] M. A. Meyers, K. K. Chawla, *Mechanical Behavior of Materials*, Cambridge University Press, Cambridge, **2009**.

[103] A. Asadpoure, L. Valdevit, *Int. J. Solids Struct.* **2015**, *60–61*, 1.

[104] V. S. Deshpande, N. a. Fleck, *Int. J. Solids Struct.* **2001**, *38*, 6275.

[105] J. Zhang, M. F. Ashby, *Int. J. Mech. Sci.* **1992**, *34*, 475.

[106] P. M. Suquet, *J. Mech. Phys. Solids* **1993**, *41*, 981.

[107] J. Bauer, A. Schroer, R. Schwaiger, I. Tesari, L. Valdevit, O. Kraft, *Extrem. Mech. Lett.* **2015**, *3*, 105.

[108] S. C. Han, J. W. Lee, K. Kang, *Adv. Mater.* **2015**, *27*, 5506.

[109] M. G. Lee, J. W. Lee, S. C. Han, K. Kang, *Acta Mater.* **2016**, *103*, 595.

[110] Hall, *Proc. Phys. Soc. B* **1951**, *64*, 747.

[111] N. J. Petch, *J. Iron Steel Inst.* **1953**, *174*, 25.

[112] X. W. Gu, Z. Wu, Y.-W. Zhang, D. J. Srolovitz, J. R. Greer, *Nano Lett.* **2013**, *13*, 5703.

[113] X. W. Gu, C. N. Loynachan, Z. Wu, Y. Zhang, D. J. Srolovitz, J. R. Greer, *Nano Lett.* **2012**, *12*, 6385.

[114] J. X. Zhao, R. C. Bradt, P. L. J. Walker, *Carbon N. Y.* **1985**, *23*, 15.

[115] A. Liu, in *ASM Handb. Vol. 19, Fatigue Fract.*, ASM International, **1996**, pp. 980–1000.

[116] M. D. Groner, F. H. Fabreguette, J. W. Elam, S. M. George, *Chem. Mater.* **2004**, *16*, 639.

[117] D. W. Richerson, *Modern Ceramic Engineering: Properties, Processing, and Use in Design*, CRC Press Taylor & Francis Group, Boca Raton, **2006**.

[118] R. Dou, B. Derby, *Scr. Mater.* **2009**, *61*, 524.

[119] H. S. Ma, J. H. Prévost, R. Jullien, G. W. Scherer, *J. Non. Cryst. Solids* **2001**, *285*, 216.

[120] H. G. Allen, P. S. Bulson, *Background To Buckling*, McGraw-Hill Book Company, **1980**.

[121] A. J. Jacobsen, W. B. Carter, S. Nutt, *Acta Mater.* **2007**, *55*, 6724.

[122] R. M. Jones, *Buckling of Bars, Plates, and Shells*, Bull Ridge Corporation, **2006**.

[123] B. Haghpanah, L. Salari-Sharif, P. Pourrajab, J. Hopkins, L. Valdevit, *Adv. Mater.* **2016**, *28*, 8065.

[124] D. Restrepo, N. D. Mankame, P. D. Zavattieri, *Extrem. Mech. Lett.* **2015**, *4*, 52.

[125] S. Shan, S. H. Kang, J. R. Raney, P. Wang, L. Fang, F. Candido, J. A. Lewis, K. Bertoldi, *Adv. Mater.* **2015**, *27*, 4296.

[126] T. Frenzel, C. Findeisen, M. Kadic, P. Gumbsch, M. Wegener, *Adv. Mater.* **2016**, 5865.

[127] M. F. Ashby, *Materials Selection in Mechanical Design Third Edition*, Butterworth-Heinemann, Oxford, **2005**.

[128] J. H. Lee, L. Wang, S. Kooi, M. C. Boyce, E. L. Thomas, *Nano Lett.* **2010**, *10*, 2592.

[129] J. H. Lee, L. F. Wang, M. C. Boyce, E. L. Thomas, *Nano Lett.* **2012**, *12*, 4392.

[130] J. H. Lee, J. P. Singer, E. L. Thomas, *Adv. Mater.* **2012**, *24*, 4782.

[131] L. Wang, M. C. Boyce, C. Y. Wen, E. L. Thomas, *Adv. Funct. Mater.* **2009**, *19*, 1343.

[132] N. A. Fleck, X. Qiu, *J. Mech. Phys. Solids* **2007**, *55*, 562.

[133] H. C. Tankasala, V. S. Deshpande, N. A. Fleck, *J. Appl. Mech.* **2015**, *82*, 91004.

[134] M. R. O'Masta, L. Dong, L. St-Pierre, H. N. G. Wadley, V. S. Deshpande, *J. Mech. Phys. Solids* **2017**, *98*, 271.

[135] L. C. Montemayor, W. H. Wong, Y.-W. Zhang, J. R. Greer, *Sci. Rep.* **2016**, *6*, 20570.

[136] D. Jang, R. Maaß, G. Wang, P. K. Liaw, J. R. Greer, *Scr. Mater.* **2013**, *68*, 773.

[137] G. N. Greaves, A. L. Greer, R. S. Lakes, T. Rouxel, *Nat Mater* **2011**, *10*, 823.

[138] K. K. Saxena, R. Das, E. P. Calius, *Adv. Eng. Mater.* **2016**, *18*, 1847.

1477 [139] J. C. Álvarez Elipe, A. Díaz Lantada, *Smart Mater. Struct.* **2012**, *21*, 105004.

1478 [140] S. Hengsbach, A. Díaz Lantada, *Smart Mater. Struct.* **2014**, *23*, 87001.

1479 [141] G. W. Milton, A. V. Cherkaev, *J. Eng. Mater. Technol.* **1995**, *117*, 483.

1480 [142] M. Kadic, T. Bückmann, R. Schittny, P. Gumbsch, M. Wegener, *Phys. Rev. Appl.*
1481   **2014**, *2*, 1.

1482 [143] M. Kadic, T. Bückmann, R. Schittny, M. Wegener, *New J. Phys.* **2013**, *15*, DOI
1483   10.1088/1367-2630/15/2/023029.

1484 [144] T. Bückmann, M. Thiel, M. Kadic, R. Schittny, M. Wegener, *Nat. Commun.* **2014**, *5*,
1485   4130.

1486 [145] D. Y. Kang, W. Lee, D. Kim, J. H. Moon, *Langmuir* **2016**, *32*, 8436.

1487 [146] J. Kaschke, M. Wegener, *Opt. Lett.* **2015**, *40*, 3986.

1488 [147] M. Elmeranta, G. Vicidomini, M. Duocastella, A. Diaspro, G. De Miguel, *Opt. Mater.*
1489   *Express* **2016**, *3*, 444.

1490 [148] J. Fischer, M. Wegener, *Opt. Mater. Express* **2011**, *1*, 614.

1491 [149] Z. Liu, X. Zhang, Y. Mao, Y. Y. Zhu, Z. Yang, C. T. Chan, P. Sheng, *Science (80-.).*
1492   **2000**, *289*, 1734.

1493 [150] S. Krödel, C. Daraio, *Phys. Rev. Appl.* **2016**, *6*, 64005.

1494 [151] M. F. Ashby, A. Evans, N. a Fleck, L. J. Gibson, J. W. Hutchinson, H. N. G. Wadley,
1495   *Metal Foams: A Design Guide*, Butterworth-Heinemann, Oxford, **2000**.

1496 [152] L. Valdevit, A. J. Jacobsen, J. R. Greer, W. B. Carter, *J. Am. Ceram. Soc.* **2011**, *1*, 1.

1497 [153] C. A. Steeves, M. Y. He, S. D. Kasen, L. Valdevit, H. N. G. Wadley, A. G. Evans, *J.*
1498   *Appl. Mech.* **2009**, *76*, 31014.

1499 [154] L. Valdevit, A. Pantano, H. A. Stone, A. G. Evans, *Int. J. Heat Mass Transf.* **2006**, *49*,
1500   3819.

1501 [155] N. G. Dou, A. J. Minnich, *Appl. Phys. Lett.* **2016**, *108*, DOI 10.1063/1.4939266.

1502 [156] R. Lakes, *Appl. Phys. Lett.* **2007**, *90*, DOI 10.1063/1.2743951.

1503 [157] O. Sigmund, S. Torquato, *J. Mech. Phys. Solids* **1997**, *45*, 1037.

1504 [158] J. B. Hopkins, K. J. Lange, C. M. Spadaccini, *J. Mech. Des.* **2013**, *135*, 61004.

1505 [159] R. M. Panas, J. B. Hopkins, *Proc. Annu. Meet. Am. Soc. Precis. Eng. 29th Annu. Meet.*
1506   **2014**, 2.

1507 [160] Q. Wang, J. A. Jackson, Q. Ge, J. B. Hopkins, C. M. Spadaccini, N. X. Fang, *Phys.*
1508   *Rev. Lett.* **2016**, *117*, 1.

1509 [161] M. C. Orilall, U. Wiesner, *Chem. Soc. Rev.* **2011**, *40*, 520.

1510 [162] D. B. Burckel, C. M. Washburn, A. K. Raub, S. R. J. Brueck, D. R. Wheeler, S. M.
1511   Brozik, R. Polsky, *Small* **2009**, *5*, 2792.

1512 [163] X. Xia, C. V. Di Leo, X. W. Gu, J. R. Greer, *ACS Energy Lett.* **2016**, *1*, 492.

1513 [164] W. . b Wang, M. . Ozkan, C. S. . b b Ozkan, *J. Mater. Chem. A* **2016**, *4*, 3356.

1514 [165] P. Danilevicius, *J. Biomed. Opt.* **2012**, *17*, 81405.

1515 [166] F. Klein, B. Richter, T. Striebel, C. M. Franz, G. Von Freymann, M. Wegener, M.
1516   Bastmeyer, *Adv. Mater.* **2011**, *23*, 1341.

1517 [167] C. Peters, M. Hoop, S. Pané, B. J. Nelson, C. Hierold, *Adv. Mater.* **2016**, *28*, 533.

1518 [168] D. W. Yee, M. D. Schulz, R. H. Grubbs, J. R. Greer, *Adv. Mater.* **2017**, 1605293.

1519 [169] H. N. G. Wadley, *Phil Trans R Soc A* **2005**, *364*, 31.

1520 [170] I. Gibson, D. W. Rosen, B. Stucker, *Additive Manufacturing Technologies*, Springer
1521   US, New York, **2015**.

1522 [171] S. Yin, A. J. Jacobsen, L. Wu, S. R. Nutt, *J. Mater. Sci.* **2013**, *48*, 6558.

1523 [172] G. S. Xu, G. Yang, J. Gong, *Adv. Mater. Res.* **2012**, *424–425*, 52.

1524 [173] B. Golaz, V. Michaud, Y. Leterrier, J. A. E. Mnson, *Polymer (Guildf).* **2012**, *53*, 2038.

1525 [174] C. E. Corcione, A. Greco, A. Maffezzoli, *Polymer (Guildf).* **2005**, *46*, 8018.

1526 [175] R. Bail, J. Y. Hong, B. D. Chin, *J. Ind. Eng. Chem.* **2016**, *38*, 141.

1527 [176] J. Choi, R. B. Wicker, S. Cho, C. Ha, S. Lee, *Rapid Prototyp. J.* **2009**, *15*, 59.

1528 [177] R. Bail, A. Patel, H. Yang, C. M. Rogers, F. R. A. J. Rose, J. I. Segal, S. M. Ratchev,
1529   *Procedia CIRP* **2013**, *5*, 222.
1530 [178] Y. De Hazan, J. Heinecke, A. Weber, T. Graule, *J. Colloid Interface Sci.* **2009**, *337*, 66.
1531 [179] J. W. Lee, I. H. Lee, D.-W. Cho, *Microelectron. Eng.* **2006**, *83*, 1253.
1532 [180] A. Badev, Y. Abouliatim, T. Chartier, L. Lecamp, P. Lebaudy, C. Chaput, C. Delage, *J.*
1533   *Photochem. Photobiol. A Chem.* **2011**, *222*, 117.
1534 [181] S. Kirihara, in *Eng. Ceram. Curr. Status Futur. Prospect.*, **2016**, pp. 117–122.
1535 [182] S. Kirihara, *Weld. World* **2016**, *60*, 697.
1536 [183] C. Kermer, M. Rasse, G. Lagogiannis, G. Undt, A. Wagner, W. Millesi, *J. Cranio-*
1537   *Maxillo-Facial Surg.* **1998**, *26*, 360.
1538 [184] B. Farkas, I. Romano, L. Ceseracciu, A. Diaspro, F. Brandi, S. Beke, *Mater. Sci. Eng.*
1539   *C* **2015**, *55*, 14.
1540 [185] A. Alibeigloo, *Compos. Part B Eng.* **2016**, *98*, 225.
1541 [186] P. Mueller, M. Thiel, M. Wegener, *Opt. Lett.* **2014**, *39*, 6847.
1542 [187] J. S. Oakdale, J. Ye, W. L. Smith, J. Biener, *Opt. Express* **2016**, *24*, 186.
1543 [188] L. J. Jiang, Y. S. Zhou, W. Xiong, Y. Gao, X. Huang, L. Jiang, T. Baldacchini, J.-F.
1544   Silvain, Y. F. Lu, *Opt. Lett.* **2014**, *39*, 3034.
1545 [189] L. Valdevit, J. Bauer, in *Three-Dimensional Microfabr. Using Two-Phot. Polym.* (Ed.:
1546   T. Baldacchini), Elsevier, Amsterdam, **2015**, pp. 345–373.
1547 [190] H. Namatsu, K. Yamazaki, K. Kurihara, *J. Vac. Sci. Technol. B Microelectron. Nanom.*
1548   *Struct.* **2000**, *18*, 780.
1549 [191] G. M. Whitesides, B. Grzybowski, *Science (80-.).* **2002**, *295*, 2418.
1550 [192] W. Bai, C. A. Ross, *MRS Bull.* **2016**, *41*, 100.
1551 [193] P. F. W. Simon, R. Ulrich, H. W. Spiess, U. Wiesner, **2001**, 3464.
1552 [194] C. A. Ross, K. K. Berggren, J. Y. Cheng, Y. S. Jung, J. B. Chang, *Adv. Mater.* **2014**,
1553   *26*, 4386.
1554 [195] M. R. J. Scherer, L. Li, P. M. S. Cunha, O. A. Scherman, U. Steiner, *Adv. Mater.* **2012**,
1555   *24*, 1217.
1556 [196] V. Z. H. Chan, J. Hoffman, V. Y. Lee, H. Iatrou, A. Avgeropoulos, N. Hadjichristidis,
1557   R. D. Miller, E. L. Thomas, *Science (80-.).* **1999**, *286*, 1716.
1558 [197] J. H. Pikul, S. Ozerinc, R. Zhang, P. V. Braun, W. P. King, *Proc. IEEE Int. Conf.*
1559   *Micro Electro Mech. Syst.* **2016**, *2016–Febru*, 451.
1560 [198] J. H. Pikul, Z. Dai, X. Yu, H. Zhang, T. Kim, P. V Braun, W. P. King, *J.*
1561   *Micromechanics Microengineering* **2014**, *24*, 105006.
1562 [199] X. Chen, L. Wang, Y. Wen, Y. Zhang, J. Wang, Y. Song, L. Jiang, D. Zhu, *J. Mater.*
1563   *Chem.* **2008**, *18*, 2262.
1564 [200] A. H. Lu, F. Schüth, *Adv. Mater.* **2006**, *18*, 1793.
1565 [201] M. H. Kim, S. H. Im, O. O. Park, *Adv. Mater.* **2005**, *17*, 2501.
1566 [202] K. P. Velikov, C. G. Christova, R. P. A. Dullens, A. van Blaaderen, *Science (80-.).*
1567   **2002**, *296*, 106.
1568 [203] R. P. Wesolowski, A. P. Terzyk, *Phys. Chem. Chem. Phys.* **2016**, *18*, 17018.
1569 [204] V. V. Mitrofanov, M. M. Slepchenkov, G. Zhang, O. E. Glukhova, *Carbon N. Y.* **2017**,
1570   *115*, 803.
1571 [205] Z. Qin, G. S. Jung, M. J. Kang, M. J. Buehler, *Sci. Adv.* **2017**, *3*, e1601536.
1572 [206] V. Varshney, S. S. Patnaik, A. K. Roy, G. Froudakis, B. L. Farmer, *ACS Nano* **2010**, *4*,
1573   1153.
1574 [207] R. K. Paul, M. Ghazinejad, M. Penchev, J. Lin, M. Ozkan, C. S. Ozkan, *Small* **2010**, *6*,
1575   2309.
1576 [208] A. J. Jacobsen, J. A. Kolodziejska, K. D. Fink, C. Zhou, C. S. Roper, W. B. Carter, in
1577   *Solid Free. Fabr. Symp. Proc.*, **2010**.
1578 [209] Nanoscribe GmbH, *Photonic Professional (GT) User Maual*, **2017**.

[210] E. J. W. Crossland, M. Kamperman, M. Nedelcu, C. Ducati, U. Wiesner, D.-M. Smilgies, G. E. S. Toombes, M. A. Hillmyer, S. Ludwigs, U. Steiner, H. J. Snaith, *Nano Lett.* **2009**, *9*, 2807.

[211] S. M. George, *Chem. Rev.* **2010**, *110*, 111.

[212] A. M. Schwartzberg, D. Olynick, *Adv. Mater.* **2015**, *27*, 5778.

[213] G. O. Mallory, J. B. Hajdu, *Electroless Plating: Fundamentals and Applications*, William Andrew Publishing, New York, **1990**.

[214] L. P. Bicelli, B. Bozzini, C. Mele, L. D'Urzo, *Int. J. Electrochem. Sci.* **2008**, *3*, 356.

[215] O. Schueller, S. Brittain, *Chem. Mater.* **1997**, *4756*, 1399.

[216] Y. Lim, J. Heo, M. Madou, H. Shin, *Nanoscale Res. Lett.* **2013**, *8*, 1.

[217] A. Mcaleavey, G. Coles, R. L. Edwards, W. N. Sharpe, *MRS Proc.* **1998**, *546*, DOI doi:10.1557/PROC-546-213.

[218] P. J. F. Harris, *Philos. Mag.* **2004**, *84*, 3159.

[219] B. Y. Ahn, S. B. Walker, S. C. Slimmer, A. Russo, A. Gupta, S. Kranz, E. B. Duoss, T. F. Malkowski, J. a Lewis, *J. Vis. Exp.* **2011**, 1.

[220] B. G. Compton, J. A. Lewis, *Adv. Mater.* **2014**, *26*, 5930.

[221] J. T. Muth, P. G. Dixon, L. Woish, L. J. Gibson, J. A. Lewis, *Proc Natl Acad Sci USA* **2017**, *114*, 1832.

[222] B. Senyuk, N. Behabtu, A. Martinez, T. Lee, D. E. Tsentalovich, G. Ceriotti, J. M. Tour, M. Pasquali, I. I. Smalyukh, *Nat. Commun.* **2015**, *6*, 7157.

[223] F. Kotz, K. Arnold, W. Bauer, D. Schild, N. Keller, K. Sachsenheimer, T. M. Nargang, C. Richter, D. Helmer, B. E. Rapp, *Nature* **2017**, *544*, 337.

[224] M. Sundaram, G. Ananthasuresh, *Resonance* **2009**, *14*, 849.

[225] A. Ajdari, B. Haghpanah Jahromi, J. Papadopoulos, H. Nayeb-hashemi, A. Vaziri, *Int. J. Solids Struct.* **2012**, *49*, 1413.

[226] B. Haghpanah, R. Oftadeh, J. Papadopoulos, A. Vaziri, *Proc. R. Soc. A Math. Phys. Eng. Sci.* **2013**, *469*, 1.

[227] R. Lakes, *Nature* **1993**, *361*, 511.

[228] G. W. Kooistra, V. S. Deshpande, H. N. G. Wadley, *J. Appl. Mech.* **2007**, *74*, 259.

[229] D. Rayneau-Kirkhope, Y. Mao, R. Farr, *Phys. Rev. Lett.* **2012**, *204301*, 1.

[230] R. Oftadeh, B. Haghpanah, D. Vella, A. Boudaoud, A. Vaziri, *Phys. Rev. Lett.* **2014**, *104301*, 1.

1613

1614 Jens Bauer received a M.S. (Dipl.-Ing.) degree in mechanical engineering from the Karlsruhe
1615 Institute of Technology (KIT), Germany, and completed his PhD at KIT's Institute for Applied
1616 Materials under Prof. Oliver Kraft. He received a research fellowship from the Deutsche
1617 Forschungsgemeinschaft (DFG) to study the multifunctional properties of nanoarchitected
1618 materials, and is currently a research associate at the University of California, Irvine working
1619 with Prof. Lorenzo Valdevit.

1620 Lucas Meza completed his M.S. and PhD at the California Institute of Technology (Caltech)
1621 under the guidance of Prof. Julia R. Greer for his research on the Mechanical Properties of 3D
1622 Nanoarchitected Materials. He is currently a research associate at the University of Cambridge
1623 studying the micromechanics of 3D woven composite materials with Prof. Vikram Deshpande.

1624 Tobias A. Schaedler is a Senior Research Scientist at HRL Laboratories, LLC, the former
1625 Hughes Research Labs in Malibu, CA, where he is developing new materials and manufacturing
1626 processes for aerospace and automotive applications. His current focus is on architected
1627 microlattices and truss core structures as well as on expanding the portfolio of ceramics and
1628 metal alloys suitable for additive manufacturing. He conducted undergraduate studies at the
1629 University of Bayreuth in Germany and then received a PhD in Materials Science from the
1630 University of California at Santa Barbara in 2006.